Thermo-elastic analysis of multilayered plates and shells based on 1D and 3D heat conduction problems

Thermo-elastic analysis of multilayered plates and shells based on 1D and 3D heat conduction problems

S. Brischetto* and R. Torre

Department of Mechanical and Aerospace Engineering, Politecnico di Torino, Torino, Italy

Abstract

The present work shows a generic 3D exact shell solution for the thermo-mechanical analysis of a heterogeneous group of one- and multi-layered isotropic, composite and sandwich structures. Plates, cylinders, cylindrical and spherical shells can be investigated using orthogonal mixed curvilinear coordinates. The 3D equilibrium equations for spherical shells automatically degenerate in those for simpler geometries. The elastic part of the proposed 3D model is based on a consolidated layer-wise exact solution which uses the exponential matrix method to solve the equilibrium differential equations through the thickness direction. The closed-form solution is obtained assuming simply-supported boundary conditions and harmonic forms for displacement and temperature fields. The temperature amplitudes are imposed at the top and bottom external surfaces in steady-state conditions. Therefore, the temperature profile can be evaluated through the thickness direction in three different ways: - calculation of the temperature profile via the steady-state 3D Fourier heat conduction equation; - evaluation of the temperature profile using the steady-state simplified 1D version of the Fourier heat conduction equation; - a priori assumed linear temperature profile through the entire thickness direction ranging from the bottom temperature value to the top temperature value. Once the temperature profile is defined at each thickness coordinate, it is considered as a known term in the 3D differential equilibrium equations. The obtained system consists in a set of non-homogeneous second order differential equilibrium equations which can be solved introducing appropriate mathematical layers. After a reduction to a first order differential equation system, the exponential matrix method is used to calculate both the general and the particular solutions. The effects of the temperature field on the static response of plates and shells are evaluated in terms of displacements and stresses. The proposed solution will be validated using reference results available in the literature. Then, new analyses will be presented for different thickness ratios, geometries, lamination schemes, materials and temperature values at the external surfaces. Results will demonstrate the importance in the 3D shell model of both the correct definition of the elastic part and the appropriate evaluation of the temperature profile through the thickness of the structure.

Keywords: 3D exact thermo-mechanical shell model; linear assumed temperature profile; 1D Fourier heat conduction equation; 3D Fourier heat conduction equation; sandwich and laminated structures; plates; shells.

*Author for Correspondence: Salvatore Brischetto, Department of Mechanical and Aerospace Engineering, Politecnico di Torino, corso Duca degli Abruzzi 24, 10129 Torino, ITALY. tel: +39.011.090.6813, fax: +39.011.090.6899, e.mail: salvatore.brischetto@polito.it.

1 Introduction

The term high-temperature structures indicates those structures subjected to severe thermal environment conditions such those related to high temperatures, high temperature gradients and cyclical changes of temperature. Some examples can be found in high-speed aircraft, spacecraft, launch vehicles, advanced propulsion systems, containment vessels for nuclear power factories and other industrial facilities such as those using high-energy-density laser beams for the production [1]- [3]. In all these cases, an appropriate structural thermal analysis must be performed. This analysis must include several features such as heat transfer problems, transient and steady-state thermal stresses, curing, processing and residual stresses, bifurcation buckling, vibrations of heated plates and shells, large deflection and postbuckling problems and analysis of plate and shell structures [3], [4]. In the case of thermal stress investigation, both the appropriate use of the mechanical modeling and the correct investigation of the thermal field are important. The mechanical modeling is strictly connected with the opportune choice of analytical or numerical 3D, 2D or 1D elements. The thermal field can be opportunely introduced in these models by means of several ways: a priori choice made for a linear assumed temperature profile through the entire thickness of the structure; resolution of the 1D version or the 3D version of the Fourier heat conduction equation in order to calculate an appropriate temperature profile through the thickness; use of uniform heat fluxes; introduction of the temperature in the elastic model as a primary variable, in analogy with the elastic variables, in order to obtain a fully coupling between the elastic and the thermal fields. The concept of fully coupled thermo-mechanical analysis was examined in depth in the past in works [5]- [11] by means of the rigorous introduction of divergence and gradient equations, constitutive relations, boundary conditions, variational principles for linear coupled thermoelasticity, field equations, proportionality law between the heat flux vector and the gradient of a scalar thermal variable, energy balance equations and the initial conditions.

In order to correctly understand the novelties of the new 3D shell model here developed for the thermal stress analysis of sandwich and composite structures, the literature survey is discussed in four different parts related to 3D exact solutions, 3D numerical models, 2D exact solutions and 2D numerical models for the thermo-mechanical investigation of one-layered and multilayered plates and shells, respectively.

In the framework of 3D exact models, Bhaskar et al. [12] presented an exact 3D plate solution with linear assumed temperature profile through the thickness. The solution was developed as a linear uncoupled thermo-elastic problem in analogy with the pure elastic solutions by Pagano [13]- [15]. The exact 3D plate solutions proposed in [16]- [18] used a calculated temperature profile through the thickness obtained from the solution of the steady-state heat conduction problem. Kulikov and Plotnikova [16] used the method of sampling surfaces. Savoia and Reddy [17] wrote the governing equations in terms of displacements for a plate composed of monoclinic layers. Tungikar and Rao [18] proposed an interesting analytical solution to obtain the temperature profile through the thickness from the solution of the 3D version of the heat conduction problem in the case of steady-state conditions, simply-supported sides and harmonic forms for the variables. Further 3D analytical models considered cylindrical shells or cylinders [19]- [22]. Alibeigloo and Zanoosi [19] proposed the static analysis of functionally graded carbon nanotube reinforced composite cylindrical shells, subjected to thermo-electro-mechanical loads, by means of governing ordinary differential equations derived by expanding the variables in terms of axial coordinate and by using the state space technique along the radial direction. Kapuria et al. [20], [21] proposed exact 3D solutions for cylindrical shells and panels in the case of thermo-electro-mechanical loads where the temperature profile was obtained from the solution of the heat conduction problem. Vel and Pelletier [22] analyzed functionally graded cylindrical shells by writing 3D equations in circumferential coordinates and by solving both the 1D and 3D Fourier heat conduction problems. In [23], the proposed analytical 3D solution for thermo-electro-elastic response of multi-layered composite cylindrical shells was obtained from a coupled thermo-electro-elastic model where the temperature is a primary

variable.

Numerical 3D models allow the investigation of boundary conditions different from the simply supported ones, and thermal and mechanical loads different from the harmonic ones. For these reasons, they are more general but also more complicated than exact 3D models. The possible inclusion of several problems connected with the numerical procedures complicates these models. Qu et al. [24] proposed a 3D boundary element method for the boundary stress analysis of plates and shells using an assumed quadratic through-the-thickness temperature profile. The 3D boundary element method proposed by Ochiai et al. [25] for plates and shells used a calculated temperature profile from the 1D heat conduction problem. Adineh and Kadkhodayan [26] developed a 3D plate solution based on the differential quadrature method using a calculated temperature profile by means of the 3D heat conduction equation. Thermal stress analysis of flat structures was conducted by Rolfes et al. [27] by means of finite difference methods or 3D finite elements for the temperature analysis, and shell elements for the stress evaluation. Works [28]- [32] are based on numerical 3D models developed in the framework of the coupled thermoelastic theory. The three-dimensional multi-field equations of functionally graded piezo-electric shells of revolution under thermo-mechanical loads were derived in [28] where the heat conduction equation and the displacement equations were developed considering thermal effects. Governing equations, which satisfied the 3D elasticity and conduction relations, were developed in [29] where the thermoelasticity analysis for laminated cylinders was proposed. Tanaka et al. [30] developed a 3D boundary element method for the coupled thermoelasticity of a 2D medium with rectilinear coordinates. Thermoelastic vibrations of free supported and clamped circular plates, caused by a thermal shock upon the plate surfaces, were analysed in [31]. The coupled system of partial differential equations was reduced to Volterra first and second kind integral equations in the time domain. Yeh [32] proposed a coupled system for thermo-mechanical vibrations of plates by means of the Galerkin method. Further interesting studies, which make use of numerical 3D models, are [33]- [35]. Three-dimensional finite element method for the thermo-mechanical stress analysis of a laminated fibre reinforced polymer composite spherical shell, subjected to an elevated thermal filed, was proposed in [33]. Kalogeropoulos et al. [34] studied an extended end-plate steel connection under elevated temperatures using three-dimensional non-linear finite elements with unilateral contact and friction interfaces. An interesting point of view was given in [35] where the problem of thermal stresses in cylindrical elastic shells was modelled as Cosserat surfaces. In the theory of Cosserat shells, the thermal effects were described by means of two temperature fields. The problem consisted in finding the equilibrium of the shell under the action of a given temperature distribution. The temperature fields were assumed to be general polynomial functions in the axial coordinate, whose coefficients depended on the circumferential coordinate.

2D shell and plate models are in general preferable to 3D shell and plate models because they have smaller computational costs even if they could present problems for thick structures or complicated lamination schemes. The partition in analytical 2D and numerical 2D models is still here valid as already seen for 3D models. In general, 2D analytical models are more accurate than the related 2D numerical models but they are less general in terms of geometries, boundary and load conditions, and lamination schemes. The 2D exact models proposed in [36]- [43] are all based on the "a priori" assumption of a temperature profile through the entire thickness. Khate et al. [36] developed 2D higher-order shear deformation theories for the thermo-mechanical analysis of simply supported doubly curved cross-ply laminated shells in the framework of the Sanders theory for doubly curved shells. The temperature profile is assumed as linear through the thickness. Ali et al. [37] proposed a new displacement-based higher order plate theory for thick laminates subjected to mechanical and thermal loads. The importance of various higher-order terms in the proposed theory was discussed using an assumed temperature profile through the thickness. Jonnalagadda et al. [38] investigated transverse shear and transverse normal strain effects in composite plates by means of a higher-order displacement field and a linear temperature profile. The state space approach was used in [39] to solve exactly the thermo-elastic governing equations of third-order, first-order and classical displacement theories

for cylindrical shells in the case of linear or constant temperature through the thickness. The same author [40] added the Reddy displacement theory and the investigation of further geometries (doubly-curved and spherical shells with linear or constant temperature profile) in the state space approach already seen in [39] for the cylindrical geometry. Murakami [41] proposed an analytical solution for the thermal bending of layered plates when the temperature was bi-sinusoidal in the plane and constant or linear through the thickness. He used a shear deformation plate theory with cubic terms for in-plane displacements. The analytical global-local higher order model in [42] allowed the thermal stress analysis of shells when the temperature was constant or linear through the thickness direction. The thermal buckling of a cylindrical FGM shell was investigated in [43] via the Donnell shell theory and a linear temperature profile through the thickness. Kapuria et al. [44] developed a higher order zigzag theory for composite and sandwich beams subjected to thermal load. The temperature was considered linear in each layer which means that the material layer effect was considered while the thickness layer effect was discarded. A calculated temperature profile from the 3D version of the Fourier heat conduction equation was included in the analytical shell model by Pelletier and Vel [45] for the the thermal stress analysis of functionally graded cylindrical shells. Analytical 2D higher order equivalent single layer (ESL) and layer wise (LW) theories were developed in [46] for multilayered shells in order to discuss the comparison between the linear assumed and the 3D calculated temperature profile through the thickness. This comparison was discussed in depth in [47] where these differences were better remarked. These higher order ESL and LW models were extended to the combination of hygrometric and thermal loads applied to plates and shells in [48] and [49], respectively. In the proposed results, assumed moisture and temperature profiles were always compared with the profiles calculated by means of the 3D Fick moisture diffusion law and the 3D Fourier heat conduction equation. The ESL and LW refined models employed in [46]- [49] for the typical thermal and/or hygroscopic stress analysis of plates and shells were extended to the fully coupled thermo-electro-elastic analysis of plates and shells (where the temperature was a primary variable of the problem directly calculated from the governing equations) in [50]- [52]. A similar fully coupled thermo-electro-elastic analysis was proposed by Cho and Oh [53] in the case of a classical 2D zigzag model for smart plates.

In the framework of 2D numerical plate and shell models, works [54]- [56] proposed assumed linear temperature profiles. Barut et al. [54] developed a non-linear Mindlin theory for a finite element thermo-elastic shell analysis. Cho et al. [55] proposed a higher-order beam type plate model for the thermal stress analyses of multilayered structures. Reddy and Hsu [56] proposed the thermal bending of composite plates via classical closed-form and finite element models. In [57], the thermal stress analysis of plates with a hole was based on a uniform heat flux. The Goodier and Florence method was used to develop this model. Librescu and Lin [58] proposed a non-linear shear deformable laminated model for flat and curved panels subjected to thermo-mechanical loads. The temperature profile was considered as linear in each layer. Works [59]- [62] solved the 1D heat transfer problem in order to calculate a temperature profile which considered the material layer effect. Miller et al. [59] proposed a Rayleigh-Ritz analysis combined with classical shell theory for the thermal stress investigation of layered cylindrical shells. Shen [60] and Shen and Noda [61], [62] proposed the post-buckling analysis of functionally graded shells, including or discarding piezoelectric layers, in the case of axial, lateral or hydrostatic loads. In papers [63]- [66], the calculated temperature profile was obtained from the solution of the 3D version of heat conduction problem in order to include both material layer and thickness layer effects. Cheng and Batra [63] developed a third-order displacement shell model with constant transverse displacement. Jabbari et al. [64] proposed a semi-analytical higher order shear deformation theory for the thermo-elastic analysis of functionally graded conical shells. Rolfes and Rohwer [65] used a temperature which was quadratic in the thickness direction where the terms were calculated via the 3D heat conduction problem. The mechanical part of the model was based on the 2D QUAD elements of Nastran. Santos et al. [66] investigated functionally graded cylindrical shells by means of a semi-analytical axisymmetric finite element model using the three-dimensional linear elasticity theory.

The three-dimensional equations of motion were reduced to two-dimensional ones by expanding the displacement field in Fourier series in the circumferential direction involving circumferential harmonics. Coupled thermo-elastic analyses were given in [67]- [71]. Daneshjo and Ramezani [67], [68] proposed a zizag theory and a third-order shear deformation theory developed in the framework of a mixed finite element model (15 degrees of freedom per node) for the dynamic coupled thermo-elastic analysis of multilayered plates. Ibrahimbegovic et al. [69] proposed a first order shear deformation theory for the finite element analysis of shells in the case of thermo-mechanical coupling. The problems of the one-dimensional axisymmetric quasi-static coupled thermoelasticity for multilayered hollow cylinders, with clamped surfaces and subjected to time-dependent boundary conditions, were proposed in [70]. The formulation was based on the basic equations of thermoelasticity in polar coordinates. Oh and Cho [71] developed a cubic zigzag finite element plate theory with full coupling between mechanical, thermal and electric fields. A three-node triangular finite element was employed. The use of commercial codes for the thermal stress analysis of structures is also common in the literature. An example was given in [72] where the finite element analysis was performed, via I-DEAS and ANSYS (using 2D shell and 3D solid elements), for thermally loaded composite tubes.

If compared to the above reference discussions, the present new 3D shell model has the following novelties. The proposed exact 3D shell model is valid for different geometries such as plates, cylinders, cylindrical shells and spherical shells which can include several isotropic, orthotropic and composite layers. The model is developed as a closed solution via the hypotheses of simply-supported sides and harmonic forms for elastic and thermal variables. The differential equations are solved via the exponential matrix method which allows the layer-wise approach and the easy imposition of equilibrium conditions and compatibility conditions. Moreover, the temperature profile can be considered in three different ways: assumed as linear through the whole thickness, calculated from the 1D version of the Fourier heat conduction equation and calculated from the 3D version of the Fourier heat conduction equation. The comparisons between these three different temperature profiles allow to evaluate the thickness layer effect and the material layer effect from the thermal point of view. In the literature, there are not exact 3D models able to investigate different geometries with the same methodology and with the opportunity of selecting three different types of temperature profile. The proposed 3D exact thermo-elastic shell model derives from the pure mechanical model already developed by the first author in [73]- [77] in the case of free vibration and bending analysis of plates and constant radii of curvature shells. The addition of the temperature profile gives non-homogeneous differential equations which can be solved via the procedure shown in [78] and [79]. When the temperature is known (assumed or calculated), the differential equations are not homogeneous any more. The 3D version of the heat conduction equation in orthogonal mixed curvilinear coordinates has been obtained from [80]- [83] and then solved in accordance with the method proposed in [18]. The new given results are presented in terms of displacements, stresses and temperature profiles. They can be used as benchmarks for the development and testing of new 3D and 2D numerical shell models implemented for the thermal stress analysis of multilayered structures.

2 3D exact thermo-mechanical shell model

The present 3D model is innovative because it considers a group of different plate and shell geometries using a general formulation. Plates, cylindrical shells, cylinders and spherical shells can be analyzed using the same model. Figures 1-4 show shells and plates in a mixed curvilinear and orthogonal reference system (α, β, z). The thickness h is constant across the structures. The origin of the reference system is located in a corner, with α and β parallel to the lateral faces and lying on the middle surface Ω_0. z is the thickness coordinate, it is normal to Ω_0 and points towards the top surface. R_α and R_β are the radii of curvature in α and β directions, respectively. They are evaluated in the middle surface Ω_0 and they are assumed to be constant. a and b are the shell dimensions in α and β directions, respectively.

They are also evaluated in the middle surface Ω_0. Three parametric coefficients are defined for each direction α, β and z:

$$H_\alpha = \left(1 + \frac{z}{R_\alpha}\right) = \left(1 + \frac{\tilde{z} - h/2}{R_\alpha}\right), \quad H_\beta = \left(1 + \frac{z}{R_\beta}\right) = \left(1 + \frac{\tilde{z} - h/2}{R_\beta}\right), \quad H_z = 1\,, \tag{1}$$

H_α and H_β depend on z (which goes from -$h/2$ to +$h/2$ with the zero positioned in the Ω_0 surface) or on $\tilde{z}$ (which varies from 0 to h and it is measured from the bottom surface). In the case of shells with constant radii of curvature, the coefficients H_α and H_β in Eq. (1) are a linear function of the thickness coordinate. For a shell with a generic stacking sequence and a number N_L of physical layers, the problem is governed by three equations of equilibrium for each k physical layer:

$$H_\beta \frac{\partial \sigma^k_{\alpha\alpha}}{\partial \alpha} + H_\alpha \frac{\partial \sigma^k_{\alpha\beta}}{\partial \beta} + H_\alpha H_\beta \frac{\partial \sigma^k_{\alpha z}}{\partial z} + (\frac{2H_\beta}{R_\alpha} + \frac{H_\alpha}{R_\beta})\sigma^k_{\alpha z} = 0, \tag{2}$$

$$H_\beta \frac{\partial \sigma^k_{\alpha\beta}}{\partial \alpha} + H_\alpha \frac{\partial \sigma^k_{\beta\beta}}{\partial \beta} + H_\alpha H_\beta \frac{\partial \sigma^k_{\beta z}}{\partial z} + (\frac{2H_\alpha}{R_\beta} + \frac{H_\beta}{R_\alpha})\sigma^k_{\beta z} = 0, \tag{3}$$

$$H_\beta \frac{\partial \sigma^k_{\alpha z}}{\partial \alpha} + H_\alpha \frac{\partial \sigma^k_{\beta z}}{\partial \beta} + H_\alpha H_\beta \frac{\partial \sigma^k_{zz}}{\partial z} - \frac{H_\beta}{R_\alpha}\sigma^k_{\alpha\alpha} - \frac{H_\alpha}{R_\beta}\sigma^k_{\beta\beta} + (\frac{H_\beta}{R_\alpha} + \frac{H_\alpha}{R_\beta})\sigma^k_{zz} = 0\,. \tag{4}$$

Eqs. (2)-(4) are valid for all the geometries presented before. The formulation is given for spherical shells with constant radii of curvature; this formulation is also valid for cylinders and cylindrical panels (when one of the two radii of curvature is ∞) and for plates (when both the radii of curvature are ∞).

The shell is subjected to a sovra-temperature field $\theta\,(\alpha,\, \beta,\, z)$, measured with respect to a reference temperature T_0 as $\theta = T - T_0$. The geometrical relations in an orthogonal mixed curvilinear reference system (α, β, z) have the following form:

$$\epsilon^k_{\alpha\alpha} = \epsilon^k_{\alpha\alpha m} - \epsilon^k_{\alpha\alpha\theta} = \frac{1}{H_\alpha}\frac{\partial u^k}{\partial \alpha} + \frac{w^k}{H_\alpha R_\alpha} - \mu^k_\alpha \theta^k\,, \tag{5}$$

$$\epsilon^k_{\beta\beta} = \epsilon^k_{\beta\beta m} - \epsilon^k_{\beta\beta\theta} = \frac{1}{H_\beta}\frac{\partial v^k}{\partial \beta} + \frac{w^k}{H_\beta R_\beta} - \mu^k_\beta \theta^k\,, \tag{6}$$

$$\epsilon^k_{zz} = \epsilon^k_{zzm} - \epsilon^k_{zz\theta} = \frac{\partial w^k}{\partial z} - \mu^k_z \theta^k\,, \tag{7}$$

$$\gamma^k_{\beta z} = \gamma^k_{\beta z m} = \frac{1}{H_\beta}\frac{\partial w^k}{\partial \beta} + \frac{\partial v^k}{\partial z} - \frac{v^k}{H_\beta R_\beta}\,, \tag{8}$$

$$\gamma^k_{\alpha z} = \gamma^k_{\alpha z m} = \frac{1}{H_\alpha}\frac{\partial w^k}{\partial \alpha} + \frac{\partial u^k}{\partial z} - \frac{u^k}{H_\alpha R_\alpha}\,, \tag{9}$$

$$\gamma^k_{\alpha\beta} = \gamma^k_{\alpha\beta m} = \frac{1}{H_\alpha}\frac{\partial v^k}{\partial \alpha} + \frac{1}{H_\beta}\frac{\partial u^k}{\partial \beta}\,, \tag{10}$$

($\epsilon^k_{\alpha\alpha}$, $\epsilon^k_{\beta\beta}$, ϵ^k_{zz}, $\gamma^k_{\beta z}$, $\gamma^k_{\alpha z}$, $\gamma^k_{\alpha\beta}$) are the six strain components for the k-th layer and they can be seen as the algebraic summation of mechanical strains (subscript m) and thermal strains (subscript θ). They are functions of the three displacement components u^k, v^k and w^k in α, β, z direction, respectively, and of the temperature θ^k by means of the coefficients of thermal expansion μ^k_α, μ^k_β and μ^k_z in the structural reference system (α, β, z). They are obtained from thermal expansion coefficients μ^k_1, μ^k_2 and μ^k_3 in the material reference system (1, 2, 3) via the opportune rotations. In order to obtain a displacement form of Eqs. (2)-(4), the constitutive equations must be introduced:

$$\boldsymbol{\sigma}^k = \boldsymbol{C}^k \boldsymbol{\epsilon}^k = \boldsymbol{C}^k(\boldsymbol{\epsilon}^k_m - \boldsymbol{\epsilon}^k_\theta)\,, \tag{11}$$

where the stress vector $\boldsymbol{\sigma}^k$ has dimension 6×1, the elastic coefficient matrix $\boldsymbol{C}^k$ has dimension 6×6 and the strains have been defined in Eqs. (5)-(10). The elastic coefficient matrix in the structural reference system (α, β, z) for an orthotropic material, with rotation angles 0° or 90°, has the form:

$$\boldsymbol{C}^k = \begin{bmatrix} C_{11}^k & C_{12}^k & C_{13}^k & 0 & 0 & 0 \\ C_{12}^k & C_{22}^k & C_{23}^k & 0 & 0 & 0 \\ C_{13}^k & C_{23}^k & C_{33}^k & 0 & 0 & 0 \\ 0 & 0 & 0 & C_{44}^k & 0 & 0 \\ 0 & 0 & 0 & 0 & C_{55}^k & 0 \\ 0 & 0 & 0 & 0 & 0 & C_{66}^k \end{bmatrix} . \tag{12}$$

The closed form solution of Eqs. (2)-(4) is obtained for orthotropic angles 0° or 90° because these simplified hypotheses allow $C_{16}^k = C_{26}^k = C_{36}^k = C_{45}^k = 0$. The explicit form of Eq. (11) in the structural reference system (α, β, z), after the substitution of the geometrical relations (5)-(10), is:

$$\sigma_{\alpha\alpha}^k = \frac{C_{11}^k}{H_\alpha} u_{,\alpha}^k + \frac{C_{11}^k}{H_\alpha R_\alpha} w^k + \frac{C_{12}^k}{H_\beta} v_{,\beta}^k + \frac{C_{12}^k}{H_\beta R_\beta} w^k + C_{13}^k w_{,z}^k - \lambda_\alpha^k \theta^k \ , \tag{13}$$

$$\sigma_{\beta\beta}^k = \frac{C_{12}^k}{H_\alpha} u_{,\alpha}^k + \frac{C_{12}^k}{H_\alpha R_\alpha} w^k + \frac{C_{22}^k}{H_\beta} v_{,\beta}^k + \frac{C_{22}^k}{H_\beta R_\beta} w^k + C_{23}^k w_{,z}^k - \lambda_\beta^k \theta^k \ , \tag{14}$$

$$\sigma_{zz}^k = \frac{C_{13}^k}{H_\alpha} u_{,\alpha}^k + \frac{C_{13}^k}{H_\alpha R_\alpha} w^k + \frac{C_{23}^k}{H_\beta} v_{,\beta}^k + \frac{C_{23}^k}{H_\beta R_\beta} w^k + C_{33}^k w_{,z}^k - \lambda_z^k \theta^k \ , \tag{15}$$

$$\sigma_{\beta z}^k = \frac{C_{44}^k}{H_\beta} w_{,\beta}^k + C_{44}^k v_{,z}^k - \frac{C_{44}^k}{H_\beta R_\beta} v^k \ , \tag{16}$$

$$\sigma_{\alpha z}^k = \frac{C_{55}^k}{H_\alpha} w_{,\alpha}^k + C_{55}^k u_{,z}^k - \frac{C_{55}^k}{H_\alpha R_\alpha} u^k \ , \tag{17}$$

$$\sigma_{\alpha\beta}^k = \frac{C_{66}^k}{H_\alpha} v_{,\alpha}^k + \frac{C_{66}^k}{H_\beta} u_{,\beta}^k \ , \tag{18}$$

where subscripts $(,\alpha)$, $(,\beta)$ and $(,z)$ indicate the related partial derivatives $(\frac{\partial}{\partial\alpha})$, $(\frac{\partial}{\partial\beta})$ and $(\frac{\partial}{\partial z})$, respectively. The thermo-mechanical coupling coefficients λ_α^k, λ_β^k and λ_3^k in Eqs. (13)-(18), defined in the structural reference system (α, β, z), are:

$$\lambda_\alpha^k = C_{11}^k \mu_\alpha^k + C_{12}^k \mu_\beta^k + C_{13}^k \mu_z^k \ , \tag{19}$$

$$\lambda_\beta^k = C_{12}^k \mu_\alpha^k + C_{22}^n \mu_\beta^k + C_{23}^k \mu_z^k \ , \tag{20}$$

$$\lambda_z^k = C_{13}^k \mu_\alpha^k + C_{23}^n \mu_\beta^k + C_{33}^k \mu_z^k \ . \tag{21}$$

A further hypothesis to obtain the closed form solution of the equilibrium equations (2)-(4) is the harmonic form for displacements and temperature which means simply supported sides. The relations for displacements are:

$$u^k(\alpha,\beta,z) = U^k(z) cos(\bar{\alpha}\alpha) sin(\bar{\beta}\beta) \ , \tag{22}$$

$$v^k(\alpha,\beta,z) = V^k(z) sin(\bar{\alpha}\alpha) cos(\bar{\beta}\beta) \ , \tag{23}$$

$$w^k(\alpha,\beta,z) = W^k(z) sin(\bar{\alpha}\alpha) sin(\bar{\beta}\beta) \ , \tag{24}$$

the two coefficients $\bar{\alpha}$ and $\bar{\beta}$ are defined as $\bar{\alpha} = \frac{m\pi}{a}$ and $\bar{\beta} = \frac{n\pi}{b}$ where a and b are the shell dimensions. m and n are the half-wave numbers in α and β directions, respectively. $U^k(z)$, $V^k(z)$ and $W^k(z)$ are the displacement amplitudes. The harmonic formulation for the temperature field is:

$$\theta^k(\alpha,\beta,z) = \Theta^k(z) sin(\bar{\alpha}\alpha) sin(\bar{\beta}\beta) \ , \tag{25}$$

where $\Theta^k(z)$ is the temperature amplitude. Introducing the harmonic form for the displacements (Eqs. (22)-(24)) and the harmonic form for the temperature (Eq. (25)) into the constitutive equations (13)-(18), and than into the equilibrium equations (2)-(4), it is possible to obtain a set of three differential equations in terms of amplitudes for the displacements and for the temperature and their related derivatives made with respect to z. The derivatives in α and β have been exactly calculated using the harmonic forms and they become known algebraic terms. Therefore, the system is now made of three differential equations of second order in z. These equations have not constant coefficients because of H_α and H_β which are functions of z. For this reason, each k physical layer is divided in a certain number of mathematical layers. Therefore, a new index j is defined for the global mathematical layers and it goes from 1 to the total number of mathematical layers M. In the middle of each j mathematical layer, the coefficients H_α and H_β are exactly calculated. In this way, coefficients A_s^j (with s from 1 to 19) and coefficients J_r^j (with r from 1 to 4) become constant parameters in the compact form of the system of differential equations in z:

$$A_1^j U^j + A_2^j V^j + A_3^j W^j + A_4^j U_{,z}^j + A_5^j W_{,z}^j + A_6^j U_{,zz}^j + J_1^j \Theta^j = 0 \,, \tag{26}$$

$$A_7^j U^j + A_8^j V^j + A_9^j W^j + A_{10}^j V_{,z}^j + A_{11}^j W_{,z}^j + A_{12}^j V_{,zz}^j + J_2^j \Theta^j = 0 \,, \tag{27}$$

$$A_{13}^j U^j + A_{14}^j V^j + A_{15}^j W^j + A_{16}^j U_{,z}^j + A_{17}^j V_{,z}^j + A_{18}^j W_{,z}^j + A_{19}^j W_{,zz}^j + J_3^j \Theta_{,z}^j + J_4^j \Theta^j = 0 \,. \tag{28}$$

Section 3 will show how the temperature profile across z can be separately calculated. This decoupling of the variables allows Eqs. (26)-(28) to become a system of second order differential equations in the displacement amplitudes U^j, V^j, W^j and their derivatives in z. The system can be reduced to a first order one using the method proposed in [84] and [85]. The order of derivatives in z can be reduced by redoubling the number of variables for each j layer from 3 (U^j, V^j, W^j) to 6 (U^j, V^j, W^j, $U^{j'}$, $V^{j'}$, $W^{j'}$). Terms Θ and Θ' are known because they will be calculated in Section 3. Superscript $'$ means derivative performed with respect to z (indicated as $\frac{\partial}{\partial z}$):

$$\begin{bmatrix} A_6^j & 0 & 0 & 0 & 0 & 0 \\ 0 & A_{12}^j & 0 & 0 & 0 & 0 \\ 0 & 0 & A_{19}^j & 0 & 0 & 0 \\ 0 & 0 & 0 & A_6^j & 0 & 0 \\ 0 & 0 & 0 & 0 & A_{12}^j & 0 \\ 0 & 0 & 0 & 0 & 0 & A_{19}^j \end{bmatrix} \begin{bmatrix} U^j \\ V^j \\ W^j \\ U^{j'} \\ V^{j'} \\ W^{j'} \end{bmatrix}' =$$

$$\begin{bmatrix} 0 & 0 & 0 & A_6^j & 0 & 0 \\ 0 & 0 & 0 & 0 & A_{12}^j & 0 \\ 0 & 0 & 0 & 0 & 0 & A_{19}^j \\ -A_1^j & -A_2^j & -A_3^j & -A_4^j & 0 & -A_5^j \\ -A_7^j & -A_8^j & -A_9^j & 0 & -A_{10}^j & -A_{11}^j \\ -A_{13}^j & -A_{14}^j & -A_{15}^j & -A_{16}^j & -A_{17}^j & -A_{18}^j \end{bmatrix} \begin{bmatrix} U^j \\ V^j \\ W^j \\ U^{j'} \\ V^{j'} \\ W^{j'} \end{bmatrix} + \begin{bmatrix} 0 & 0 & 0 & 0 & 0 & 0 \\ 0 & 0 & 0 & 0 & 0 & 0 \\ 0 & 0 & 0 & 0 & 0 & 0 \\ -J_1^j & 0 & 0 & 0 & 0 & 0 \\ -J_2^j & 0 & 0 & 0 & 0 & 0 \\ -J_4^j & -J_3^j & 0 & 0 & 0 & 0 \end{bmatrix} \begin{bmatrix} \Theta^j \\ \Theta^{j'} \\ 0 \\ 0 \\ 0 \\ 0 \end{bmatrix} , \tag{29}$$

Eq. (29) can be compacted as:

$$\boldsymbol{D}^j \boldsymbol{U}^{j'} = \boldsymbol{A}^j \boldsymbol{U}^j + \boldsymbol{J}^j \boldsymbol{\Theta}^j \,, \tag{30}$$

where $\boldsymbol{U}^j = [U^j \; V^j \; W^j \; U^{j'} \; V^{j'} \; W^{j'}]^T$, $\boldsymbol{U}^{j'} = \frac{\partial \boldsymbol{U}^j}{\partial z}$ and $\boldsymbol{\Theta}^j = [\Theta^j \; \Theta^{j'} \; 0 \; 0 \; 0 \; 0]^T$. T means the transpose of a vector. A further development of Eq. (30) is:

$$\boldsymbol{U}^{j'} = \boldsymbol{D}^{j^{-1}} \boldsymbol{A}^j \boldsymbol{U}^j + \boldsymbol{D}^{j^{-1}} \boldsymbol{J}^j \boldsymbol{\Theta}^j \,, \tag{31}$$

$$\boldsymbol{U}^{j'} = \boldsymbol{A}^{*j} \boldsymbol{U}^j + \boldsymbol{J}^{*j} \boldsymbol{\Theta}^j \,, \tag{32}$$

with $\boldsymbol{A}^{*^j} = \boldsymbol{D}^{j^{-1}}\boldsymbol{A}^j$ and $\boldsymbol{J}^{*^j} = \boldsymbol{D}^{j^{-1}}\boldsymbol{J}^j$. The implementation of the present solution into a Matlab code is simple when the temperature is assumed to be linear in each j mathematical layer. The following expression is assumed:

$$\Theta^j(\tilde{z}^j) = a_\Theta^j \tilde{z}^j + b_\Theta^j \,, \tag{33}$$

where a_Θ^j and b_Θ^j are constant within each j-th layer. $\tilde{z}^j$ is the local thickness coordinate defined inside each j mathematical layer. It varies from *0* at the bottom of the generic j-th layer to h^j at its top, where h^j is the thickness of the considered j-th layer. Section 3 shows how the coefficients a_Θ^j and b_Θ^j can be determined for each j-th layer. Eq. (32) is a system of first order differential equations in $\tilde{z}$ or z; the equations are not homogeneous because of the thermal term $\boldsymbol{J}^{*^j}\boldsymbol{\Theta}^j$ which is a function of $\tilde{z}^j$ or z^j.

A generic set of non-homogeneous first order differential equations can be written as:

$$\frac{\mathrm{d}\boldsymbol{x}}{\mathrm{d}t} = \boldsymbol{A}\boldsymbol{x} + \boldsymbol{f}(t) \,, \tag{34}$$

where $\boldsymbol{x}$ is a $M \times 1$ vector, $\boldsymbol{A}$ is a $M \times M$ matrix with constant coefficients and $\boldsymbol{f}(t) = [f_1(t) \,...\, f_M(t)]^T$ is a known function vector. Eq. (34) can be solved as:

$$\boldsymbol{x}(t) = \mathrm{e}^{\boldsymbol{A}(t-t_0)}\boldsymbol{x}_0 + \int_{t_0}^{t} \mathrm{e}^{\boldsymbol{A}(t-s)}\boldsymbol{f}(s)ds \,. \tag{35}$$

The known term in Eq. (32) can be written in explicit form as:

$$\boldsymbol{\Theta}^{*^j} = \boldsymbol{J}^{*^j}\boldsymbol{\Theta}^j = \begin{bmatrix} 0 & 0 & 0 & 0 & 0 & 0 \\ 0 & 0 & 0 & 0 & 0 & 0 \\ 0 & 0 & 0 & 0 & 0 & 0 \\ -J_1^{*^j} & 0 & 0 & 0 & 0 & 0 \\ -J_2^{*^j} & 0 & 0 & 0 & 0 & 0 \\ -J_4^{*^j} & -J_3^{*^j} & 0 & 0 & 0 & 0 \end{bmatrix} \begin{bmatrix} a_\Theta^j \tilde{z}^j + b_\Theta^j \\ a_\Theta^j \\ 0 \\ 0 \\ 0 \\ 0 \end{bmatrix} = \begin{bmatrix} 0 \\ 0 \\ 0 \\ -J_1^{*^j}(a_\Theta^j \tilde{z}^j + b_\Theta^j) \\ -J_2^{*^j}(a_\Theta^j \tilde{z}^j + b_\Theta^j) \\ -J_4^{*^j}(a_\Theta^j \tilde{z}^j + b_\Theta^j) - J_3^{*^j} a_\Theta^j \end{bmatrix} . \tag{36}$$

Therefore, Eq. (32) can be re-written in the form:

$$\boldsymbol{U}^{j'} = \boldsymbol{A}^{*^j}\boldsymbol{U}^j + \boldsymbol{\Theta}^{*^j} \,, \tag{37}$$

with $\boldsymbol{\Theta}^{*^j}$ containing only linear known functions of $\tilde{z}^j$. The solution of Eq. (37) is:

$$\boldsymbol{U}^j(\tilde{z}^j) = \mathrm{e}^{(\boldsymbol{A}^{*^j}\tilde{z}^j)}\boldsymbol{U}^j(0) + \int_0^{\tilde{z}^j} \mathrm{e}^{(\boldsymbol{A}^{*^j}(\tilde{z}^j - s))}\boldsymbol{\Theta}^{*^j}(s)ds \,. \tag{38}$$

Eq. (38) can be used to calculate the displacement vector at the top of the j-th layer once the terms $\boldsymbol{A}^{**^j} = \mathrm{e}^{(\boldsymbol{A}^{*^j}h^j)}$ and $\boldsymbol{J}^{**^j} = \int_0^{h^j} \mathrm{e}^{(\boldsymbol{A}^{*^j}(h^j - s))}\boldsymbol{\Theta}^{*^j}(s)ds$ have been evaluated for each j layer of thickness h^j. The exponential matrix can be expanded and evaluated in each j layer with thickness h^j as:

$$\boldsymbol{A}^{**^j} = \mathrm{e}^{(\boldsymbol{A}^{*^j}h^j)} = \boldsymbol{I} + \boldsymbol{A}^{*^j}h^j + \frac{\boldsymbol{A}^{*^j\,2}}{2!}h^{j\,2} + \frac{\boldsymbol{A}^{*^j\,3}}{3!}h^{j\,3} + \cdots + \frac{\boldsymbol{A}^{*^j\,N}}{N!}h^{j\,N} \,, \tag{39}$$

where $\boldsymbol{I}$ is the 6×6 identity matrix. The integral, which represents the second term in Eq. (38), is calculated for each j layer of thickness h^j by expanding the exponential matrix with the same methodology and the same order N seen in Eq. (39):

$$\boldsymbol{J}^{**^j} = \int_0^{h^j} \mathrm{e}^{(\boldsymbol{A}^{*^j}(h^j - s))}\boldsymbol{\Theta}^{*^j}(s)ds = \int_0^{h^j} \Big(\boldsymbol{I} + \boldsymbol{A}^{*^j}(h^j - s) + \frac{\boldsymbol{A}^{*^j\,2}}{2!}(h^j - s)^2 + \frac{\boldsymbol{A}^{*^j\,3}}{3!}(h^j - s)^3 + \cdots + \frac{\boldsymbol{A}^{*^j\,N}}{N!}(h^j - s)^N\Big)\boldsymbol{\Theta}^{*^j}(s)ds \,. \tag{40}$$

Therefore, using Eqs. (39) and (40), Eq. (38) becomes:

$$\boldsymbol{U}^j(h^j) = \boldsymbol{A}^{**^j}\boldsymbol{U}^j(0) + \boldsymbol{J}^{**^j}\,, \tag{41}$$

which can also be rewritten as:

$$\boldsymbol{U}_t^j = \boldsymbol{A}^{**^j}\boldsymbol{U}_b^j + \boldsymbol{J}^{**^j}\,, \tag{42}$$

indicating $\boldsymbol{U}^j(h^j)$ as $\boldsymbol{U}_t^j$ and $\boldsymbol{U}^j(0)$ as $\boldsymbol{U}_b^j$, where t and b mean top and bottom of the j layer, respectively.

Eq. (42) links the top and bottom displacements (and the relative derivatives in z) inside the same mathematical j layer. Then, a set of inter-laminar conditions must be enforced. The continuity of the displacements at each interface can be imposed as:

$$u_b^j = u_t^{j-1}\,,\;\; v_b^j = v_t^{j-1}\,,\;\; w_b^j = w_t^{j-1}\,. \tag{43}$$

The conditions expressed in Eqs. (43) can be easily elaborated for the displacement amplitudes U^j, V^j and W^j. The continuity of transverse shear and transverse normal stresses is a further condition that should be satisfied:

$$\sigma_{zz_b}^j = \sigma_{zz_t}^{j-1}\,,\;\; \sigma_{\alpha z_b}^j = \sigma_{\alpha z_t}^{j-1}\,,\;\; \sigma_{\beta z_b}^j = \sigma_{\beta z_t}^{j-1}\,. \tag{44}$$

In Eqs. (43) and (44), for each given variable, the equivalence is imposed between its value at the bottom (b) of the generic j-th layer and its value at the top (t) of the $(j-1)$-th layer. Introducing the constitutive equations (13)-(18) and the harmonic form for the displacements, it is possible to obtain a displacement form of Eqs. (43) and (44). The method is the same seen in [73]- [77], the only difference lyes in the continuity equation for the normal stress σ_{zz} where an additional thermal term is now present (see the coefficient T_{11}). The displacements form of Eqs. (43) and (44) may be rewritten in matrix compact form introducing two transfer matrices:

$$\begin{bmatrix} U \\ V \\ W \\ U' \\ V' \\ W' \end{bmatrix}_b^j = \begin{bmatrix} 1 & 0 & 0 & 0 & 0 & 0 \\ 0 & 1 & 0 & 0 & 0 & 0 \\ 0 & 0 & 1 & 0 & 0 & 0 \\ T_1 & 0 & T_2 & T_3 & 0 & 0 \\ 0 & T_4 & T_5 & 0 & T_6 & 0 \\ T_7 & T_8 & T_9 & 0 & 0 & T_{10} \end{bmatrix}^{j-1,j} \begin{bmatrix} U \\ V \\ W \\ U' \\ V' \\ W' \end{bmatrix}_t^{j-1} + \begin{bmatrix} 0 & 0 & 0 & 0 & 0 & 0 \\ 0 & 0 & 0 & 0 & 0 & 0 \\ 0 & 0 & 0 & 0 & 0 & 0 \\ 0 & 0 & 0 & 0 & 0 & 0 \\ 0 & 0 & 0 & 0 & 0 & 0 \\ T_{11} & 0 & 0 & 0 & 0 & 0 \end{bmatrix}^{j-1,j} \begin{bmatrix} \Theta \\ \Theta' \\ 0 \\ 0 \\ 0 \\ 0 \end{bmatrix}_t^{j-1}\,. \tag{45}$$

The diagonal part including 1 indicates the continuity of displacements in Eq. (43). Coefficients from T_1 to T_{11} indicate the stress continuity of Eq. (44) in terms of displacements and temperature (and their derivatives in z). A further compact form of Eq. (45) is:

$$\boldsymbol{U}_b^j = \boldsymbol{T}_U^{j-1,j}\boldsymbol{U}_t^{j-1} + \boldsymbol{T}_\Theta^{j-1,j}\boldsymbol{\Theta}_t^{j-1}\,. \tag{46}$$

Eq. (46) allows to link displacements and their derivatives in z calculated at the bottom of the j layer with displacements and temperature (and also their derivatives in z) evaluated at the top of the (j-1) layer.

The shells taken into consideration are supposed to be simply supported, and this condition is automatically satisfied by the harmonic forms used for all the variables:

$$w = v = 0,\;\; \sigma_{\alpha\alpha} = 0 \quad \text{for} \quad \alpha = 0, a\,, \tag{47}$$

$$w = u = 0,\;\; \sigma_{\beta\beta} = 0 \quad \text{for} \quad \beta = 0, b\,. \tag{48}$$

No mechanical loads are applied at the top and bottom surfaces of the shell. As seen in [73]- [77], these conditions can be rewritten in displacement form as:

$$\boldsymbol{B}_t^M\boldsymbol{U}_t^M = \boldsymbol{P}_t^M = \boldsymbol{0}\,, \tag{49}$$

$$\boldsymbol{B}_b^1\boldsymbol{U}_b^1 = \boldsymbol{P}_b^1 = \boldsymbol{0}\,, \tag{50}$$

subscripts t and b mean top and bottom, respectively. Superscript M indicates the last mathematical layer and superscript 1 indicates the first layer. Vector $\boldsymbol{P}$ contains the mechanical loads in the three direction α, β and z and it is set equal zero in the present thermal stress analysis. Matrices $\boldsymbol{B}$ allow the imposition of mechanical loads at the external surfaces. The explicit form of $\boldsymbol{P}$ and $\boldsymbol{B}$ can be found in [73]- [77].

In oder to group Eq. (49) and Eq. (50) into an algebraic system in matrix form, it was useful to express $\boldsymbol{U}_t^M = \boldsymbol{U}^M(h^M)$ in terms of $\boldsymbol{U}_b^1 = \boldsymbol{U}^1(0)$ (displacements and their derivatives in $\tilde{z}$ at the top of the last layer linked with the displacements and their derivatives in $\tilde{z}$ at the bottom of the first layer). This operation can be achieved introducing recursively Eq. (46) into Eq. (42):

$$
\begin{aligned}
\boldsymbol{U}_t^M = & \left(\boldsymbol{A}^{**M} \boldsymbol{T}_U^{M-1,M} \boldsymbol{A}^{**M-1} \boldsymbol{T}_U^{M-2,M-1} ..... \boldsymbol{A}^{**2} \boldsymbol{T}_U^{1,2} \boldsymbol{A}^{**1} \right) \boldsymbol{U}_b^1 + \\
& \left(\boldsymbol{A}^{**M} \boldsymbol{T}_U^{M-1,M} \boldsymbol{A}^{**M-1} ..... \boldsymbol{A}^{**2} \boldsymbol{T}_U^{1,2} \boldsymbol{J}^{**1} + \right. \\
& \boldsymbol{A}^{**M} \boldsymbol{T}_U^{M-1,M} \boldsymbol{A}^{**M-1} ..... \boldsymbol{A}^{**3} \boldsymbol{T}_U^{2,3} \boldsymbol{J}^{**2} + \\
& \vdots \\
& \boldsymbol{A}^{**M} \boldsymbol{T}_U^{M-1,M} \boldsymbol{J}^{**M-1} + \\
& \boldsymbol{J}^{**M} + \\
& \boldsymbol{A}^{**M} \boldsymbol{T}_U^{M-1,M} \boldsymbol{A}^{**M} ..... \boldsymbol{A}^{**2} \boldsymbol{T}_\Theta^{1,2} \boldsymbol{\Theta}_t^1 + \\
& \boldsymbol{A}^{**M} \boldsymbol{T}_U^{M-1,M} \boldsymbol{A}^{**M} ..... \boldsymbol{A}^{**3} \boldsymbol{T}_\Theta^{2,3} \boldsymbol{\Theta}_t^2 + \\
& \vdots \\
& \boldsymbol{A}^{**M} \boldsymbol{T}_U^{M-1,M} \boldsymbol{A}^{**M-1} \boldsymbol{T}_\Theta^{M-2,M-1} \boldsymbol{\Theta}_t^{M-2} + \\
& \left. \boldsymbol{A}^{**M} \boldsymbol{T}_\Theta^{M-1,M} \boldsymbol{\Theta}_t^{M-1} \right) .
\end{aligned}
\tag{51}
$$

The first block of Eq. (51) in brackets defines the 6×6 matrix $\boldsymbol{H}_m$ for multilayered structures already seen in [73]- [77] for the pure mechanical analysis. M terms including $\boldsymbol{J}^{**j}$ (which explicitly contain the thermal profile within each j mathematical layer) and $M-1$ terms including $\boldsymbol{\Theta}_t^j$ (which identify the temperature at each interface) are added. The summation of all the quantities in the second block in brackets in Eq. (51) defines the 6×1 vector $\boldsymbol{H}_\Theta$:

$$
\boldsymbol{U}_t^M = \boldsymbol{H}_m \boldsymbol{U}_b^1 + \boldsymbol{H}_\Theta \, . \tag{52}
$$

Using Eq. (52), it is possible to rewrite Eq. (49) in terms of $\boldsymbol{U}_b^1$:

$$
\boldsymbol{B}_t^M \boldsymbol{H}_m \boldsymbol{U}_b^1 = -\boldsymbol{B}_t^M \boldsymbol{H}_\Theta \, . \tag{53}
$$

Eqs. (53) and (50) can be now compacted as:

$$
\boldsymbol{E} \boldsymbol{U}_b^1 = \boldsymbol{P}_\Theta \, , \tag{54}
$$

where

$$
\boldsymbol{E} = \begin{bmatrix} \boldsymbol{B}_t^M \boldsymbol{H}_m \\ \boldsymbol{B}_b^1 \end{bmatrix} \tag{55}
$$

and

$$\boldsymbol{P}_\Theta = \begin{bmatrix} -\boldsymbol{B}_t^M \boldsymbol{H}_\Theta \\ \boldsymbol{0} \end{bmatrix} . \tag{56}$$

Matrix $\boldsymbol{E}$ has always 6×6 dimension independently by the number M of mathematical layers and even if the method uses a layer wise approach. This matrix does not change with respect to the pure mechanical analysis in [73]- [77]. The load vector $\boldsymbol{P}_\Theta$ now contains only equivalent thermal loads. The system in Eq. (54) is formally the same shown in [73]- [77] for the pure mechanical analysis: the thermal field has been converted in an equivalent load $\boldsymbol{P}_\Theta$ with dimension 6×1 (the first three lines can be different from zero).

Once the bottom displacements have been calculated from Eq.(54), Eqs. (46) and Eq. (42) can be subsequently used in order to evaluate the displacements (and their derivatives with respect to z) through the entire thickness of the multilayered structure.

3 Heat conduction problem

In Section 2, the temperature profile through the thickness coordinate must be separately calculated. The shell is subjected to a temperature field with imposed amplitudes Θ_t at the top and Θ_b at the bottom. The temperature profile can be defined in three different ways: resolution of the 3D version of the Fourier heat conduction equation (θ_c,3D), by solving the 1D version of the Fourier heat conduction equation (θ_c,1D), and a priori linear assumed temperature profile for the entire multilayered structure (θ_a).

3.1 3D Fourier heat conduction equation

In a general orthogonal curvilinear coordinate system (u_1, u_2, u_3), the differential equation of heat conduction for a stationary and homogeneous solid, without internal energy generation, is:

$$\nabla \cdot \boldsymbol{q}(u_1, u_2, u_3) = 0 . \tag{57}$$

When the coordinate system is orthogonal and curvilinear, the divergence of the heat flux may be written as:

$$\nabla \cdot \boldsymbol{q} = \frac{1}{a}\left[\frac{\partial}{\partial u_1}\left(\frac{a}{a_1}q_1\right) + \frac{\partial}{\partial u_2}\left(\frac{a}{a_2}q_2\right) + \frac{\partial}{\partial u_3}\left(\frac{a}{a_3}q_3\right)\right] , \tag{58}$$

q_1, q_2, q_3 are the heat flux components in 1, 2 and 3 directions, respectively:

$$q_i = -\kappa_i \frac{1}{a_i}\frac{\partial \theta}{\partial u_i} , \tag{59}$$

where κ_i are the coefficients of thermal conductivity in u_i direction. a_1, a_2 and a_3 are the so-called scale factors, and a is defined as:

$$a = a_1\, a_2\, a_3 . \tag{60}$$

Povstenko [81] showed that Eq. (58) can be rewritten in a mixed curvilinear orthogonal coordinate system (α, β, z) for an orthotropic material as:

$$\frac{1}{H_\alpha H_\beta}\left[\frac{\partial}{\partial \alpha}\left(\frac{H_\alpha H_\beta}{H_\alpha}\kappa_1 \frac{1}{H_\alpha}\frac{\partial \theta}{\partial \alpha}\right) + \frac{\partial}{\partial \beta}\left(\frac{H_\alpha H_\beta}{H_\beta}\kappa_2 \frac{1}{H_\beta}\frac{\partial \theta}{\partial \beta}\right)\right] + \kappa_3 \frac{\partial^2 \theta}{\partial z^2} = 0 \ , \tag{61}$$

where z is rectilinear and $H_z = 1$. As shown by Leissa [86], the scale factors a_i coincide with the parametric coefficients defined in Eq. (1):

$$a_1 = H_\alpha, \ a_2 = H_\beta, \ a_3 = H_z = 1 . \tag{62}$$

The three heat fluxes have been defined in Eqs. (58) and (59). Using Eq. (61), for a generic physical orthotropic layer k, the differential operators are then transferred only to the temperature field:

$$\kappa_1^{*k}(z)\frac{\partial^2\theta}{\partial\alpha^2}+\kappa_2^{*k}(z)\frac{\partial^2\theta}{\partial\beta^2}+\kappa_3^{*k}(z)\frac{\partial^2\theta}{\partial z^2}=0\,. \tag{63}$$

with

$$\kappa_1^{*k}(z)=\frac{\kappa_1^k}{H_\alpha^2},\quad \kappa_2^{*k}(z)=\frac{\kappa_2^k}{H_\beta^2},\quad \kappa_3^{*k}(z)=\kappa_3^k\,. \tag{64}$$

Eq. (63) has not constant coefficients because in κ_1^{*k} and κ_2^{*k}, H_α and H_β are functions of z. Dividing the shell into j mathematical layers, it is possible to obtain M equations, one for each j mathematical layer, with constant coefficients κ_1^{*j}, κ_3^{*j} and κ_3^{*j} calculated in the middle of each j layer. Therefore, Eq.(63), including non constant coefficients, can be rewritten as an equation with constant coefficients:

$$\kappa_1^{*j}\frac{\partial^2\theta}{\partial\alpha^2}+\kappa_2^{*j}\frac{\partial^2\theta}{\partial\beta^2}+\kappa_3^{*j}\frac{\partial^2\theta}{\partial z^2}=0\,. \tag{65}$$

Eq. (65) is automatically satisfied by the harmonic form for the temperature $\theta(\alpha,\beta,z)$ seen in Eq. (25) where the dependence of the amplitude $\Theta(z)$ from the thickness coordinate z is assumed to be:

$$\Theta^j(z)=\Theta_0^j\exp(s^jz)\,, \tag{66}$$

where both Θ_0^j and s^j must be determined for each j-th mathematical layer. s^j can be easily determined substituting Eq. (25), with the assumption of Eq. (66), into Eq. (65):

$$s_{1,2}^j=\pm\sqrt{\frac{\kappa_1^{*j}\bar{\alpha}^2+\kappa_2^{*j}\bar{\beta}^2}{\kappa_3^{*j}}}\,, \tag{67}$$

s_1^j has been chosen as solution (algebraic sign +), and Eq. (66) can be rewritten as:

$$\Theta^j(z)=\Theta_{01}^j\exp(s_1^jz)+\Theta_{02}^j\exp(s_1^jz)\,, \tag{68}$$

$$\Theta^j(z)=S_1^jcosh(s_1^jz)+S_2^jsinh(s_1^jz)\,. \tag{69}$$

Both Eqs. (68) and (69) contain some parameters to be determined for each j mathematical layer. s_1^j for each j-th layer can be calculated using Eq. (67). $2\times M$ coefficients need to be determined. This result can be achieved as two continuity conditions at each layer interface:

$$\Theta_b^{(j+1)}=\Theta_t^j\,, \tag{70}$$

$$\kappa_3^{*j+1}\Theta_{,z_b}^{(j+1)}=\kappa_3^{*j}\Theta_{,z_t}^j\,. \tag{71}$$

Eq. (70) states that the temperature at the top of the generic j-th layer must be equal to the one at the bottom of the $(j+1)$-th layer. Eq. (71) implies the equivalence of the heath flux q_3 in the thickness direction 3 when evaluated at the bottom (b) of the $(j+1)$-th layer and at the top (t) of the j-th layer. Developing Eqs. (70) and (71), using the expression of Θ^j given in Eq. (69), it is possible to express in a compact matrix form the link existing between S_1 and S_2 at the j-th layer and S_1 and S_2 at the $(j+1)$-th layer:

$$\begin{bmatrix}S_1\\S_2\end{bmatrix}^{j+1}=\begin{bmatrix}V_{\Theta_1}^{j+1,j} & V_{\Theta_2}^{j+1,j}\\ V_{\Theta_3}^{j+1,j} & V_{\Theta_4}^{j+1,j}\end{bmatrix}\begin{bmatrix}S_1\\S_2\end{bmatrix}^{j}\,. \tag{72}$$

A total number of $2 \times (M-1)$ conditions can be imposed where $(M-1)$ is the number of layer interfaces. Defining the transfer matrix of Eq. (72) as $\boldsymbol{V}_{\Theta}^{(j+1,j)}$, the link between the coefficients at the top layer ($j = M$) and those at the bottom layer ($j = 1$) can be found using recursively Eq. (72):

$$\begin{bmatrix} S_1 \\ S_2 \end{bmatrix}^M = \boldsymbol{V}_{\Theta}^{(M,M-1)} \boldsymbol{V}_{\Theta}^{(M-1,M-2)} ..... \boldsymbol{V}_{\Theta}^{(3,2)} \boldsymbol{V}_{\Theta}^{(2,1)} \begin{bmatrix} S_1 \\ S_2 \end{bmatrix}^1 = \boldsymbol{V}_{\Theta}^{(M,1)} \begin{bmatrix} S_1 \\ S_2 \end{bmatrix}^1 . \tag{73}$$

The problem in Eqs. (73) can be solved imposing the temperatures at the bottom and at the top of the shell for the 2 conditions missed in the $2 \times (M-1)$ conditions already imposed in Eq.(72). Therefore, all the $2 \times M$ coefficients (S_1^j and S_2^j for all the M mathematical layers) can be calculated. Once the coefficients of the external layers have been determined, the remaining coefficients can be consequently calculated.

As stated in Section 2 the implementation of this solution is easier if the temperature is assumed to be linear within each mathematical layer. Once the coefficients of Eq. (69) have been determined for each j mathematical layer, the temperature profile across the thickness is completely determined. Both the coefficients presented in Eq. (33) can be determined: b_{Θ}^j represents the temperature value at the bottom of the j-th layer, while a_{Θ}^j is the slope of the temperature profile in the considered j layer. The 3D exact shell model of Section 2 which uses this temperature profile is called as 3D(θ_c,3D).

3.2 1D Fourier heat conduction equation

Even if the physics of the problem is three-dimensional, when the thickness ratio a/h and/or b/h is high enough, the determination of the temperature profile can be further simplified. The in-plane behavior of the temperature is completely determined as the thermal field has the harmonic expression presented in Eq. (25). For the k-th physical layer the three heat fluxes take the following form:

$$q_1^k = \kappa_1^{*k} \bar{\alpha} \Theta^k(z) cos(\bar{\alpha}\alpha) sin(\bar{\beta}\beta) \, , \tag{74}$$

$$q_2^k = \kappa_2^{*k} \bar{\beta} \Theta^k(z) sin(\bar{\alpha}\alpha) cos(\bar{\beta}\beta) \, , \tag{75}$$

$$q_3^k = \kappa_3^{*k} \Theta_{,z}^k(z) sin(\bar{\alpha}\alpha) sin(\bar{\beta}\beta) \, . \tag{76}$$

For high values of thickness ratios, Eqs. (61) and (63) can be simplified as:

$$\frac{\partial}{\partial z} \left(\kappa_3^* \frac{\partial \Theta}{\partial z} \right) = 0 \, , \tag{77}$$

where $\kappa_3^* = \kappa_3$ because z is rectilinear. This feature is due to the fact that heat fluxes q_1 and q_2 decrease when the thickness ratio increases. Therefore, they can be discarded. The content in the bracket in Eq. (77) represents the heat flux in the thickness direction for the entire structure. Eq. (77) implies that $q_3(z)$ is assumed to be constant through the entire thickness of the multilayered structure:

$$q_3(z) = \left(\kappa_3^* \frac{\partial \Theta}{\partial z} \right) = const \, . \tag{78}$$

Eq. (78) means that the heat flux q_3 is constant in all the multilayered structure. Eq. (78) can be also used to write the continuity of heat flux q_3 at each interface between two adjacent physical layers k or mathematical layers j. Taking as example the generic j-th mathematical layer, the differential operator can be simplified and written in algebraic form which indicates the slope of the temperature profile:

$$q_3^j = -\kappa_3^{*j} \frac{\partial \Theta^j}{\partial z} = -\frac{\kappa_3^{*j}}{h^j} (\Theta_t^j - \Theta_b^j) \, . \tag{79}$$

The term κ_3^{*j}/h^j is the thermal conductance of the j-th layer. The constant heat flux flowing through the thickness can be calculated defining the equivalent thermal resistance coefficient of the entire structure (in analogy with the electric resistance):

$$R_{z_{eq}} = \sum_{j=1}^{M} \frac{h^j}{\kappa_3^{*j}} \,. \tag{80}$$

Once the equivalent thermal resistance of the entire structure has been found, the heat flux q_3 for the whole structure can be calculated using a single equivalent layer:

$$q_3 = -\frac{1}{R_{z_{eq}}}(\Theta_t - \Theta_b) = const. \tag{81}$$

where Θ_t and Θ_b are the applied sovra-temperature amplitudes at the external surfaces of the whole structure. The temperature at any coordinate z can be therefore obtained using the continuity of q_3^j as written in Eq. (79):

$$q_3^j = -\kappa_3^{*j}\frac{(\Theta_t^j - \Theta_b^j)}{h^j} = q_3^{j+1} = -\kappa_3^{*j+1}\frac{(\Theta_t^{j+1} - \Theta_b^{j+1})}{h^{j+1}} = q_3 = const.\,, \tag{82}$$

if the coefficient κ_3^{*j} changes passing from a layer to another adjacent layer, the continuity of q_3^j is allowed by the change of the slope of the temperature profile $\frac{(\Theta_t^j - \Theta_b^j)}{h^j}$. Therefore, when the material of the layer changes, the slope of the temperature profile also changes but it remains linear in the layer. In fact, this method allows to see the material layer effect but not the thickness layer effect. This approach allows to consider only the stacking sequence and the material effects; the three dimensionality of the problem is neglected and also the thickness layer effect. This model is able to see the change of conductivity κ_3^* in each layer and the related slope of the temperature. However, the temperature remains linear in each layer even if the layer is thick. The thickness layer effect (temperature profile not linear in the thick layer) is only captured by the 3D Fourier heat conduction equation in Subsection 3.1. As seen in Subsection 3.1, the two coefficients of Eq. (33) (b_Θ^j and a_Θ^j) are the temperature value at the bottom of the j-th layer and the slope of the temperature profile in it. The transition from the physical k to the mathematical j layer was obvious as already explained in subsection 3.1. The 3D exact shell model of Section 2 which uses this temperature profile is called as 3D(θ_c,1D).

3.3 A priori linear assumed temperature profile

A further simplification can be made considering the temperature profile as linear through the entire thickness of the structure from the bottom to the top without considering the change of the material in each layer. It is a common hypothesis present in the literature. This assumption is justified when the shell has high thickness ratios and the stacking sequence includes a single layer or several thermally homogeneous layers. The coefficients of Eq. (33) can be determined as seen before: a_Θ^j is even easier to be determined in this case because it is just the global slope of the temperature profile. The 3D exact shell model of Section 2 which uses this temperature profile is called as 3D(θ_a).

4 Results

This section is organized in two main parts. In the first part, three assessments are presented in order to validate the proposed 3D exact general shell model. Comparisons with other results found in the literature are proposed to understand the opportune choice of N order of expansion for the exponential matrix in Eqs. (39) and (40) and the appropriate M number of mathematical layers for the calculation

of curvature terms and temperature profiles. After these preliminary assessments, the model can be considered as validated and it can be used to propose new results. New results are shown in the second part, after the opportune choice of N and M parameters. The 3D shell model is used to discuss the effects of geometry (plates, cylinders, cylindrical and spherical shells), thickness ratio, lamination scheme, material, temperature impositions and temperature profiles in the 3D thermo-elastic analysis of plate and shells.

4.1 Preliminary assessments

Three different preliminary assessments are here proposed to validate the new 3D general exact shell model. A square plate, a cylindrical shell and a spherical shell are investigated considering different thickness ratios, lamination schemes, materials and temperature profiles. After these assessments, the new 3D shell model is validated: $N = 3$ order of expansion for the exponential matrix and $M = 300$ mathematical layers are always sufficient to obtain a correct 3D thermo-elastic analysis for all the new benchmarks proposed in the Section 4.2. Preliminary considerations about the "a priori" assumption or the calculation of temperature profiles will be here given, even if these features will be discussed in depth in the second part about the new results where graphical evaluations of the temperature through the thickness direction will be also proposed.

The first assessment considers a simply-supported square plate ($a = b$) with thickness $h = 1$. The bi-sinusoidal ($m = n = 1$) sovra-temperature is imposed at the external surfaces at the top (t) as $\Theta_t = +1K$ and at the bottom (b) as $\Theta_b = -1K$. The three-layered composite plate has lamination sequence $0°/90°/0°$ and thickness layers $h_1 = h_2 = h_3 = h/3$. The elastic properties of each composite layer are $E_L/E_T = 25$, $G_{LT}/E_T = 0.5$, $G_{TT}/E_T = 0.2$ and $\nu_{LT} = \nu_{TT} = 0.25$ where E indicates the Young modulus, G is the shear modulus and ν is the Poisson ratio. Subscript T indicates the in-plane and out-of-plane transverse directions, while the subscript L indicates the longitudinal direction along the fibers. The thermal expansion coefficients have a ratio $\mu_T/\mu_L = 1125$. The conductivity coefficients are $\kappa_L = 36.42W/mK$ and $\kappa_T = 0.96W/mK$. The reference results are based on the the thermoelastic solution for orthotropic and anisotropic composite laminates proposed by Bhaskar et al. [12] using a priori assumed linear temperature profile through the thickness of the plate (θ_a). The new proposed 3D shell model can employ a priori assumed linear temperature profile through the thickness (θ_a), a calculated temperature profile through the thickness using the 1D version of the Fourier heat conduction equation (θ_c,1D) or a calculated temperature profile through the thickness using the 3D version of the Fourier heat conduction equation (θ_c,3D). The exact 3D general shell model uses an order of expansion $N = 3$ for the calculation of the exponential matrix and a certain number of mathematical layers M for the calculation of curvature terms (in the case of shell geometries) and the evaluation of the temperature profile through the thickness by means of fixed points. Table 1 shows the transverse displacement and in-plane normal and in-plane shear stresses for different thickness ratios a/h. The present 3D model based on an assumed linear temperature profile (θ_a) is in accordance with the reference solution [12] because this last reference also uses an assumed linear temperature profile. Only for the very thick plate (a/h=2), it is necessary the use of a number of mathematical layers greater than 100. For all the other thickness ratios, $M = 100$ is always sufficient. The calculated temperature profile by means of the 1D version of the Fourier heat conduction equation (θ_c,1D) is able to consider only the material layer effects and not the thickness layer effects. However, in this case, the change of lamination scheme does not modify the properties in the z direction and for this reason the 3D(θ_c,1D) model does not show any material layer effect and it is always coincident with the case of assumed linear temperature profile (3D(θ_a)). In the case of temperature profile calculated by means of the 3D version of Fourier heat conduction equation (3D(θ_c,3D)), the thickness layer effect is clearly shown because these results are completely different from those obtained via 3D(θ_a) and 3D(θ_c,1D) models. The three proposed 3D exact models are coincident only for thin and moderately thin plates (thickness ratios a/h greater

than 50).

The second assessment shows a simply-supported cylindrical shell with radii of curvature $R_\alpha = 10m$ and $R_\beta = \infty$, and dimensions $a = \frac{\pi}{3}R_\alpha$ and $b = 1m$. The bi-sinusoidal ($m = n = 1$) sovra-temperature is imposed at the external surfaces at the top (t) as $\Theta_t = +1K$ and at the bottom (b) as $\Theta_b = 0K$. The two-layered isotropic cylindrical shell has thickness layers $h_1 = h_2 = h/2$. The bottom layer is made of Aluminium Alloy (Al2024) and the top layer is made of Titanium Alloy (Ti22). The bottom layer has Young modulus $E = 73GPa$, Poisson ratio $\nu = 0.3$, thermal expansion coefficient $\mu = 25\times10^{-6}1/K$ and conductivity coefficient $\kappa = 130W/mK$. The top layer has Young modulus $E = 110GPa$, Poisson ratio $\nu = 0.32$, thermal expansion coefficient $\mu = 8.6\times10^{-6}1/K$ and conductivity coefficient $\kappa = 21.9W/mK$. The reference results are based on the higher order layer wise models (quasi-3D description of thermal and elastic variables) proposed in [50]. The employed reference solutions can describe the temperature field as an external load which has been a priori assumed as linear through the thickness (θ_a) or as a primary variable of the problem (in analogy with the displacement) which can be calculated from the solution of the governing equations (in this case the symbol θ_M is used to remark that the temperature has been modelled (M) and calculated from the employed 2D model). The new proposed exact 3D general shell model has all the characteristics already described for the first assessment. Table 2 shows transverse and in-plane displacements for different thickness ratios R_α/h. $M = 100$ mathematical layers are always sufficient to obtain correct results for each thickness ratio and temperature profile. In this assessment, the two layers are completely different from the elastic and thermal point of view. For this reason, the linear assumed temperature profile is always different from the calculated temperature profile even when the shell is very thin. This feature is due to the fact that the material layer effects are always present for both thick and thin shells. The 3D(θ_a) model is always coincident with the reference solution Ref.(θ_a) [50] because both use always an assumed linear temperature profile. The 3D(θ_c,3D) model is always coincident with the reference solution Ref.(θ_M) [50] because both use a 3D temperature profile (obtained from the 3D version of the Fourier heat conduction equation in the first case, and from the fully coupled thermo-elastic governing equations in the second case). The 3D(θ_c,1D) model, which uses the 1D version of the Fourier heat conduction equation, is coincident with the 3D(θ_c,3D) model for thin shells because the material layer effects are considered by both the models. In the case of thick shells, some differences are shown (in particular for the in-plane displacements) because the 3D(θ_c,1D) model is not able to see the thickness layer effects as done by the 3D(θ_c,3D) model.

The third assessment proposes a simply-supported spherical shell with radii of curvature $R_\alpha = R_\beta = R$ and dimensions $a = b = 1$. The global thickness is $h = 0.1$ which means a thickness ratio $a/h = 10$. The bi-sinusoidal ($m = n = 1$) sovra-temperature is imposed at the external surfaces at the top (t) as $\Theta_t = +0.5K$ and at the bottom (b) as $\Theta_b = -0.5K$. The two-layered composite spherical shell has lamination sequence $0°/90°$ and thickness layers $h_1 = h_2 = h/2$. The elastic properties of each composite layer are Young modulus $E_1 = 25$ and $E_2 = E_3 = 1$, shear modulus $G_{12} = G_{13} = 0.5$ and $G_{23} = 0.2$, Poisson ratio $\nu_{12} = \nu_{13} = \nu_{23} = 0.25$, thermal expansion coefficients $\mu_1 = \mu_3 = 1$ and $\mu_2 = 3$. Conductivity coefficients are $\kappa_1 = 36.42W/mK$ and $\kappa_2 = \kappa_3 = 0.96W/mK$. The no-dimensional transverse displacement is given as $\bar{w} = \frac{10h}{b^2\mu_1 T_1}w$ where $T_1 = 1K$ is the temperature gradient. The reference results are based on the higher order two-dimensional theory proposed in [36] which uses an assumed linear temperature profile (θ_a). The new proposed exact 3D general shell model has all the characteristics already described for the first and second assessments. Table 3 shows transverse displacement for different thickness ratios. The 3D(θ_a) model is always similar to the reference solution [36] because both models use an assumed linear temperature profile, even if the Ref.(θ_a) [36] model is not refined enough. $M = 100$ mathematical layers are always sufficient to obtain correct results for each possible thickness ratio and temperature profile. The 3D(θ_c,1D) and 3D(θ_c,3D) models have the same behavior already discussed for the Table 1 about the first assessment. Only the 3D(θ_c,3D) model is able to show the thickness layer effects.

The new benchmarks in the next part consider different geometries, thickness ratios, lamination

schemes, materials, temperature profiles and variable investigations (displacements and stresses). For this reason, even if the preliminary assessments have demonstrated that $M = 100$ mathematical layers could be sufficient for quite all the cases, the conservative choice of $M = 300$ mathematical layers combined with $N = 3$ order of expansion will be employed for the new benchmarks.

4.2 New results

Eight new benchmarks are here proposed considering plates, cylinders, cylindrical panels and spherical panels as geometries. Different temperature impositions (also considering different half-wave numbers) will be considered (see Figures 1-4 for further details about geometry and temperature imposition). Different lamination schemes and materials for the layers will be employed. Therefore, a one-layer and a multi-layer configuration will be investigated for each possible geometry. Linear assumed temperature profiles (3D(θ_a)), calculated temperature profiles through the thickness using the 1D version of the Fourier heat conduction equation (3D(θ_c,1D)), and calculated temperature profiles through the thickness using the 3D version of the Fourier heat conduction equation (3D(θ_c,3D)) will be used. For all the proposed 3D solutions, $N = 3$ order of expansion for the exponential matrix and $M = 300$ mathematical layers will be used (see the preliminary assessments in the previous section). Thanks these features, a complete thermal stress analysis will be proposed and these results will be valid benchmarks for those scientists involved in the developing of 2D and 3D analytical and numerical shell and plate models.

The first benchmark proposes a simply-supported square ($a = b$) one-layered composite plate with fibre orientation 0° (see Figure 1). The global thickness is $h = 1m$ and the investigated thickness ratios are $a/h = 2, 5, 10, 20, 50, 100$. The sovra-temperature in bi-sinusoidal form (half-wave numbers $m = n = 1$) has amplitude value at the top $\Theta_t = +0.5K$ and at the bottom $\Theta_b = -0.5K$. The composite material has Young modulus $E_1 = 172.72GPa$ and $E_2 = E_3 = 6.909GPa$, shear modulus $G_{12} = G_{13} = 3.45GPa$ and $G_{23} = 1.38GPa$, Poisson ratio $\nu_{12} = \nu_{13} = \nu_{23} = 0.25$, thermal expansion coefficients $\mu_1 = 0.57 \times 10^{-6}1/K$ and $\mu_2 = \mu_3 = 35.6 \times 10^{-6}1/K$ and conductivity coefficients $\kappa_1 = 36.42W/mK$ and $\kappa_2 = \kappa_3 = 0.96W/mK$. Figure 5 proposes the temperature profile through the thickness for a thick and a thin plate. In the case of a thin one-layered orthotropic plate, assumed linear (θ_a), calculated via 1D Fourier heat conduction equation (θ_c,1D) and calculated via 3D Fourier heat conduction equation (θ_c,3D) temperature profiles are coincident. In the case of thick plate, the calculated temperature profile via 3D Fourier heat conduction equation (θ_c,3D) has a different behavior through the thickness because it is able to include the thickness layer effect. Table 4 shows the three displacement components and the six stress components in particular positions through the thickness direction for different thickness ratios. In the case of very thin plates, the three proposed 3D models are coincident because both thickness layer and material layer effects are absent. For thick or moderately thick plates, the 3D models using the assumed temperature profile 3D(θ_a) and the 1D calculated temperature profile 3D(θ_c,1D) are coincident because both cannot evaluate the thickness layer effect. The 3D(θ_c,3D) model gives different results because it is able to see the thickness layer effect thanks the use of the 3D version of the Fourier heat conduction equation. Figure 6 shows the three displacement components and three stress components through the thickness in the case of thick plate (a/h=10). In-plane displacements are not linear and transverse displacement is not constant because of the high thickness value. In-plane stresses are continuous because only one layer is considered. The transverse normal stress satisfies the external load conditions.

The second benchmark investigates a simply-supported square ($a = b$) three-layered ($h_1 = h_2 = h_3 = h/3$) composite plate with fibre orientations 0°/90°/0° (see Figure 1). The global thickness h, the thickness ratios a/h, the applied sovra-temperature and the elastic and thermal properties of the composite layers are the same already described for the first benchmark. The temperature profiles through the thickness proposed in Figure 7 do not change with respect to the one-layered case because

the plate is square and when the fiber orientation changes from 0° to 90°, the conductivity coefficient κ_3 remains the same, and even if the conductivity coefficients κ_1 and κ_2 are exchanged, they multiply the same side (a=b) and half-wave numbers (m=n) in the solution of the 3D version of the Fourier heat conduction equation. Table 5 shows the results in terms of displacements and stresses for this second benchmark. For thin plates, the three 3D models are very close while for thicker plates the 3D(θ_c,3D) shows bigger differences because it is able to consider the thickness layer effects. Figure 8 gives the displacements and stresses for a thick three-layered plate. In-plane displacements show the typical zigzag form of multilayered orthotropic structures and the transverse displacement is not constant because of the thicker configuration. Displacements are continuous at each layer interface because of the correct imposition of the congruence conditions. In-plane stress $\sigma_{\alpha\alpha}$ is discontinuous at each layer interface. The transverse normal stress σ_{zz} is continuous because of the correct imposition of the equilibrium conditions.

The third benchmark shows a simply supported isotropic one-layered cylinder. The radii of curvature are $R_\alpha = 10m$ and $R_\beta = \infty$, the dimensions are $a = 2\pi R_\alpha$ and $b = 30m$ (see Figure 2). The investigated thickness ratios are $R_\alpha/h = 2, 5, 10, 20, 50, 100$ with global thickness indicated as h. The sovra-temperature in harmonic form (half-wave numbers $m = 2$ and $n = 1$) has amplitude value at the top $\Theta_t = +0.5K$ and at the bottom $\Theta_b = -0.5K$. The isotropic layer is made of Aluminium Alloy Al2024 with Young modulus $E = 73GPa$, Poisson ratio $\nu = 0.3$, thermal expansion coefficient $\mu = 25 \times 10^{-6} 1/K$ and conductivity coefficient $\kappa = 130W/mK$. The three types of temperature profile are given in Figure 9 for thick and thin cylinder. In this case, the thickness layer effect is not evident for the thicker cylinder because of the symmetry of the closed and circular geometry. These considerations remain valid in the discussion of displacements and stresses in Table 6 where 3D(θ_a) model, 3D(θ_c,1D) model and 3D(θ_c,3D) model are coincident for thin cylinders. Very small differences are shown for very thick cylinders: in this last case the thickness layer effect captured by the 3D(θ_c,3D) model is not significative. This feature is maybe due to the great rigidity of the closed cylinder. Figure 10 shows displacement and stress evaluations through the thickness which are typical of one-layered isotropic cylinders. The analyzed cylinder is thick and for this reason in-plane displacements are not linear and transverse normal displacement is not constant. Transverse shear and transverse normal stresses satisfy the external load conditions.

The fourth benchmark considers a simply supported isotropic two-layered cylinder. The global thickness h, the geometry features, the thickness ratios R_α/h and the applied sovra-temperatures are the same already described for the third benchmark (see Figure 2). In this fourth case, the two layers have the same thickness $h_1 = h_2 = h/2$. The bottom layer is made of the Aluminium Alloy Al2024 already described in the previous benchmark. The top layer is made of Titanium Alloy Ti22 with Young modulus $E = 110GPa$, Poisson ratio $\nu = 0.32$, thermal expansion coefficient $\mu = 8.6 \times 10^{-6} 1/K$ and conductivity coefficient $\kappa = 21.9W/mK$. The results in Figure 11 show as the temperature profile is never linear for all the structure even if the cylinder is thin. This feature is due to the different thermal properties considered for the two involved layers. The thick cylinder shows a small thickness layer effect because of the same reasons already discussed in the third benchmark. Displacements and stresses for different thickness rations R_α/h are proposed in Table 7 where it is evident how the results obtained via the 3D(θ_a) model are always not correct because the temperature profile is never linear through the entire thickness structure (even if the cylinder is very thin). Displacement and stress evaluations through the thickness given in Figure 12 for a thick two-layered cylinder show the effects of the two different layers. Displacements and transverse shear/normal stresses are continuous because the compatibility and equilibrium conditions have been correctly imposed in the model. In-plane stress has a discontinuity at the interface between the Al2024 layer and the Ti22 layer.

The fifth benchmark analyses a simply supported isotropic one-layered cylindrical shell. The radii of curvature are $R_\alpha = 10m$ and $R_\beta = \infty$, the dimensions are $a = \frac{\pi}{3} R_\alpha$ and $b = 20m$ (see Figure 3). The investigated thickness ratios are $R_\alpha/h = 2, 5, 10, 20, 50, 100$ with global thickness indicated

as h. The sovra-temperature in cylindrical bending form (half-wave numbers $m = 1$ and $n = 0$) has amplitude value at the top $\Theta_t = +1.0K$ and at the bottom $\Theta_b = 0.0K$. The isotropic layer is made of Titanium Alloy Ti22 with Young modulus $E = 110GPa$, Poisson ratio $\nu = 0.32$, thermal expansion coefficient $\mu = 8.6 \times 10^{-6} 1/K$ and conductivity coefficient $\kappa = 21.9W/mK$. The three temperature profiles in Figure 13 are coincident for thin shell because of the only isotropic layer. In the case of thick shell, the calculated temperature profile via the resolution of the 3D Fourier heat conduction equation is different from the linear behavior because of the thickness layer effect. This behavior is confirmed by the displacement and stress results proposed in Table 8 for different thickness ratios: the three proposed 3D models are very similar for thin structure. The applied temperature has a cylindrical bending form and for this reason displacement v and stresses $\sigma_{\alpha\beta}$ and $\sigma_{\beta z}$ are zero at each position through the thickness. Figure 14 shows the displacements and stresses different from zero in the case of thick cylindrical shell. The typical features connected with the investigation of only one isotropic layer and a very thick shell are clearly shown.

The sixth benchmark is devoted to the thermal stress analysis of a sandwich cylindrical shell with a PVC core and two external isotropic Al2024 skins. The global thickness h, the geometry features, the thickness ratios R_α/h and the applied sovra-temperature are the same already described for the fifth benchmark (see Figure 3). The external skins have thickness $h_1 = h_3 = 0.1h$ and the internal soft core has thickness $h_2 = 0.8h$. The elastic and thermal properties of the Al2024 alloy have already been given for the benchmarks 3 and 4. The PVC has Young modulus $E = 3GPa$, Poisson ratio $\nu = 0.4$, thermal expansion coefficient $\mu = 50 \times 10^{-6} 1/K$ and conductivity coefficient $\kappa = 0.18W/mK$. Results shown in Figure 15 demonstrate how the calculation of the temperature profile is fundamental for both thick and thin sandwich structures. The temperature profile is never linear because of the great differences between the thermal properties of the skins and those of the core. In the case of thick sandwich shell, the calculated temperature profile via the 1D Fourier equation is not able to capture the thickness layer effects (in fact, it is linear inside each considered layer). The differences between the three types of temperature profile become clear in Table 9 in terms of displacements and stresses at different thickness positions for several thickness ratios. The 3D(θ_c,1D) and 3D(θ_c,3D) models give very similar results for thin shells while they show important differences for thick shells. Results obtained via the 3D(θ_a) model are always wrong. Displacement u and stresses $\sigma_{\alpha\beta}$ and $\sigma_{\beta z}$ are always zero because of m=0 half-wave number in the imposed temperature profile. Figure 16 for thick sandwich shell (R_α/h=10) shows the typical zigzag form of displacements and stresses for sandwich structures. In-plane stresses show discontinuities at each interface between skin and core. Transverse shear and transverse normal stresses are continuous at each interface because of the correct imposition for the equilibrium conditions. These stresses also satisfy the external boundary load conditions.

The seventh benchmark considers a simply-supported isotropic one-layered spherical shell. The radii of curvature are $R_\alpha = R_\beta = 10m$, the dimensions are $a = \frac{\pi}{3} R_\alpha = b = \frac{\pi}{3} R_\beta$ (see Figure 4). The investigated thickness ratios are $R_\alpha/h = 2, 5, 10, 20, 50, 100$ with global thickness indicated as h. The sovra-temperature in bi-sinusoidal form (half-wave numbers $m = n = 1$) has amplitude value at the top $\Theta_t = +1.0K$ and at the bottom $\Theta_b = 0.0K$. The isotropic layer is made of Steel with Young modulus $E = 210GPa$, Poisson ratio $\nu = 0.3$, thermal expansion coefficient $\mu = 12 \times 10^{-6} 1/K$ and conductivity coefficient $\kappa = 60W/mK$. Temperature profiles in Figure 17 show how the temperature behavior is linear through the thickness in the case of thin shell. On the contrary, the temperature must be calculated via the 3D Fourier heat conduction equation in the case of thick shell because the thickness layer effect must be included. These considerations are confirmed by the displacement and stress results given in Table 10 where 3D(θ_c,1D) and 3D(θ_a) models are always coincident for each thickness ratio and investigated variable. 3D(θ_c,3D) is coincident with the other two models for thin shells, while it gives different results for thicker shells because of the thickness layer effect. Figure 18 shows the typical displacement and stress evaluations through the thickness of a thick one-layered isotropic spherical shell.

The eighth and last benchmark analyses a simply-supported isotropic three-layered spherical shell. The global thickness h, the geometry features, the thickness ratios R_α/h and the applied sovra-temperature are the same already described for the seventh benchmark (see Figure 4). The three layers have thickness $h_1 = h_2 = h_3 = h/3$ and the lamination scheme from the bottom to the top is Al2024/Ti22/Steel. The elastic and thermal properties of the three employed materials have already been given in the previous benchmark descriptions. Figure 19 shows how the temperature profile must be always calculated for each thickness ratio because the three layers have different thermal properties. In the case of thick shells, both thickness layer and material layer effects are present and the use of the 3D Fourier heat conduction equation is mandatory. These considerations are confirmed by the results in terms of displacements and stresses proposed in Table 11. The use of an assumed linear temperature profile is always inadequate, while the use of the 1D Fourier heat conduction equation shows some limits in the case of very thick shells. Only the 3D(θ_c,3D) model always guarantees the correct results for each thickness ratio, lamination scheme, material layer and investigated variable. In the results proposed for the thick shell (R_α/h=10) in Figure 20, the typical zigzag form of investigated variables through the thickness, due to a high transverse anisotropy, is shown. Moreover, compatibility conditions for displacements and equilibrium conditions for transverse shear/normal stresses have been correctly imposed in the model.

5 Conclusions

A general 3D exact shell solution for the thermo-mechanical analysis of one-layered and multilayered isotropic, sandwich and composite plates and shells have been proposed. The temperature amplitudes have been imposed at the top and bottom external surfaces in steady state conditions and then evaluated through the thickness direction. Three different methodologies have been used to define the temperature profile through the thickness: - calculation of the temperature profile via the steady-state 3D Fourier heat conduction equation which gives the 3D(θ_c,3D) model; - evaluation of the temperature profile using the steady-state simplified 1D version of the Fourier heat conduction equation which gives the 3D(θ_c,1D) model; - a priori assumed linear temperature profile through the entire thickness direction ranging from the bottom temperature value to the top temperature value which gives the 3D(θ_a) model. The 3D calculated temperature profile allows to consider both thickness layer and material layer effects, while the 1D calculated temperature profile is only able to evaluate the material layer effect. The "a priori" linear assumption for the temperature profile is only valid for thin and one-layered structures. Several analyses, in terms of displacements, in-plane and out-of-plane stresses and temperature profiles have been presented for different thickness ratios, geometries, lamination schemes, materials and temperature impositions. These results showed the importance of both the correct definition of the elastic part in the 3D shell model and the correct evaluation of the temperature profile through the thickness of the structure. In fact, even if a very refined 3D shell model is employed, wrong thermo-mechanical responses can be obtained if the temperature profile through the thickness is not coherently defined.

References

[1] L. Librescu and P. Marzocca, Thermal stresses '03, vol. 1, Blacksburg (VA, USA): Virginia Polytechnic Institute and State University, 2003.

[2] L. Librescu and P. Marzocca, Thermal stresses '03, vol. 2, Blacksburg (VA, USA): Virginia Polytechnic Institute and State University, 2003.

[3] A.K. Noor and W.S. Burton, Computational models for high-temperature multilayered composite plates and shells, *Applied Mechanics Reviews*, 45, 419-446, 1992.

[4] J.L. Nowinski, Theory of Thermoelasticity with Applications, The Netherlands: Sijthoff & Noordhoff, 1978.

[5] G.A. Altay and M.C. Dökmeci, Fundamental variational equations of discontinuous thermopiezoelectric fields, *International Journal of Engineering Science*, 34, 769-782, 1996.

[6] G.A. Altay and M.C. Dökmeci, Some variational principles for linear coupled thermoelasticity, *International Journal of Solids and Structures*, 33, 3937-3948, 1996.

[7] G.A. Altay and M.C. Dökmeci, Coupled thermoelastic shell equations with second sound for high-frequency vibrations of temperature-dependent materials, *International Journal of Solids and Structures*, 38, 2737-2768, 2001.

[8] A.A. Cannarozzi and F. Ubertini, A mixed variational method for linear coupled thermoelastic analysis, *International Journal of Solids and Structures*, 38, 717-739, 2001.

[9] N.C. Das, S.N. Das and B. Das, Eigenvalue approach to thermoelasticity, *Journal of Thermal Stresses*, 6, 35-43, 1983.

[10] W. Kosnski and K. Frischmuth, Thermomechanical coupled waves in a nonlinear medium, *Wave Motion*, 34, 131-141, 2001.

[11] J. Wauer, Free and forced magneto-thermo-elastic vibrations in a conducting plate layer, *Journal of Thermal Stresses*, 19, 671-691, 1996.

[12] K. Bhaskar, T.K. Varadan and J.S.M. Ali, Thermoelastic solution for orthotropic and anisotropic composite laminates, *Composites. Part B: Engineering*, 27, 415-420, 1996.

[13] N.J. Pagano, Exact solutions for composite laminates in cylindrical bending, *Journal of Composite Materials*, 3, 398-411, 1969.

[14] N.J. Pagano, Exact solutions for rectangular bidirectional composites and sandwich plates, *Journal of Composite Materials*, 4, 20-34, 1970.

[15] N.J. Pagano and A.S.D. Wang, Further study of composite laminates under cylindrical bending, *Journal of Composite Materials*, 5, 521-528, 1971.

[16] G.M. Kulikov and S.V. Plotnikova, Three-dimensional thermal stress analysis of laminated composite plates with general layups by a sampling surfaces method, *European Journal of Mechanics A/Solids*, 49, 214-226, 2015.

[17] M. Savoia and J.N. Reddy, Three-dimensional thermal analysis of laminated composite plates, *International Journal of Solids and Structures*, 32, 593-608, 1995.

[18] V.B. Tungikar and K.M. Rao, Three dimensional exact solution of thermal stresses in rectangular composite laminate, *Composite Structures*, 27, 419-430, 1994.

[19] A. Alibeigloo and A.A. Pasha Zanoosi, Thermo-electro-elasticity solution of functionally graded carbon nanotube reinforced composite cylindrical shell embedded in piezoelectric layers, *Composite Structures*, 173, 268-280, 2017.

[20] S. Kapuria, S. Sengupta and P. C. Dumir, Three-dimensional solution for a hybrid cylindrical shell under axisymmetric thermoelectric load, *Archive of Applied Mechanics*, 67, 320-330, 1997.

[21] S. Kapuria, S. Sengupta and P.C. Dumir, Three-dimensional piezothermoelastic solution for shape control of cylindrical panel, *Journal of Thermal Stresses*, 20, 67-85, 1997.

[22] S.S. Vel and J.L. Pelletier, Multi-objective optimization of functionally graded thick shells for thermal loading, *Composite Structures*, 81, 386-400, 2007.

[23] K. Xu and A.K. Noor, Three-dimensional analytical solutions for coupled thermoelectroelastic response of multi-layered cylindrical shells, *AIAA Journal*, 34, 802-812, 1996.

[24] W. Qu, Y. Zhang, Y. Gu and F. Wang, Three-dimensional thermal stress analysis using the indirect BEM in conjunction with the radial integration method, *Advances in Engineering Software*, 112, 147-153, 2017.

[25] Y. Ochiai, V. Sladek and J. Sladek, Three-dimensional unsteady thermal stress analysis by triple-reciprocity boundary element method, *Engineering Analysis with Boundary Elements*, 37, 116-127, 2013.

[26] M. Adineh and M. Kadkhodayan, Three-dimensional thermo-elastic analysis and dynamic response of a multi-directional functionally graded skew plate on elastic foundation, *Composites. Part B: Engineering*, 125, 227-240, 2017.

[27] R. Rolfes, J. Noack and M. Taeschner, High performance 3D-analysis of thermo-mechanically loaded composite structures, *Composite Structures*, 46, 367-379, 1999.

[28] M. Dehghan, M.Z. Nejad and A. Moosaie, Thermo-electro-elastic analysis of functionally graded piezoelectric shells of revolution: governing equations and solutions for some simple cases, *International Journal of Engineering Science*, 104, 34-61, 2016.

[29] J. Padovan, Thermoelasticity of cylindrically anisotropic generally laminated cylinders, *Journal of Applied Mechanics*, 43, 124-130, 1976.

[30] M. Tanaka, T. Matsumoto and M. Moradi, Application of boundary element method to 3-D problems of coupled thermoelasticity, *Engineering Analysis with Boundary Elements*, 16, 297-303, 1995.

[31] D. Trajkovski and R. Cukic, A coupled problem of thermoelastic vibrations of a circular plate with exact boundary conditions, *Mechanics Research Communications*, 26, 217-224, 1999.

[32] Y.-L. Yeh, The effect of thermo-mechanical coupling for a simply supported orthotropic rectangular plate on non-linear dynamics, *Thin-Walled Structures*, 43, 1277-1295, 2005.

[33] R.R. Das, A. Singla and S. Srivastava, Thermo-mechanical interlaminar stress and dynamic stability analysis of composite spherical shells, *Procedia Engineering*, 144, 1060-1066, 2016.

[34] A. Kalogeropoulos, G.A. Drosopoulos and G.E. Stavroulakis, Thermal-stress analysis of a three-dimensional end-plate steel joint, *Construction and Building Materials*, 29, 619-626, 2012.

[35] M. Bîrsan, Thermal stresses in cylindrical Cosserat elastic shells, *European Journal of Mechanics A/Solids*, 28, 94-101, 2009.

[36] R.K. Khare, T. Kant and A.K. Garg, Closed-form thermo-mechanical solutions of higher-order theories of cross-ply laminated shallow shells, *Composite Structures*, 59, 313-340, 2003.

[37] J.S.M. Ali, K. Bhaskar and T.K. Varadan, A new theory for accurate thermal/mechanical flexural analysis of symmetric laminated plates, *Composite Structures*, 45, 227-232, 1999.

[38] K.D. Jonnalagadda, T.R. Tauchert and G.E. Blandford, High-order thermoleastic composite plate theories: an analytic comparison, *Journal of Thermal Stresses*, 16, 265-285, 1993.

[39] A.A. Khdeir, Thermoelastic analysis of cross-ply laminated circular cylindrical shells, *International Journal of Solids and Structures*, 33, 4007-4016, 1996.

[40] A.A. Khdeir, M.D. Rajab and J.N. Reddy, Thermal effects on the response of cross-ply laminated shallow shells, *International Journal of Solids and Structures*, 29, 653-667, 1992.

[41] H. Murakami, Assessment of plate theories for treating the thermomechanical response of layered plates, *Composites Engineering*, 3, 137-149, 1993.

[42] W. Zhen and C. Wanji, A global-local higher order theory for multilayered shells and the analysis of laminated cylindrical shell panels, *Composite Structures*, 84, 350-361, 2008.

[43] L. Wu, Z. Jiang and J. Liu, Thermoelastic stability of functionally graded cylindrical shells, *Composite Structures*, 70, 60-68, 2005.

[44] S. Kapuria, P.C. Dumir and A. Ahmed, An efficient higher order zigzag theory for composite and sandwich beams subjected to thermal loading, *International Journal of Solids and Structures*, 40, 6613-6631, 2003.

[45] J.L. Pelletier and S.S. Vel, An exact solution for the steady-state thermoelastic response of functionally graded orthotropic cylindrical shells, *International Journal of Solids and Structures*, 43, 1131-1158, 2006.

[46] S. Brischetto, Effect of the through-the-thickness temperature distribution on the response of layered and composite shells, *International Journal of Applied Mechanics*, 1, 581-605, 2009.

[47] S. Brischetto and E. Carrera, Heat conduction and thermal analysis in multilayered plates and shells, *Mechanics Research Communications*, 38, 449-455, 2011.

[48] S. Brischetto, Hygrothermal loading effects in bending analysis of multilayered composite plates, *CMES: Computer Modeling in Engineering & Sciences*, 88, 367-417, 2012.

[49] S. Brischetto, Hygrothermoelastic analysis of multilayered composite and sandwich shells, *Journal of Sandwich Structures and Materials*, 15, 168-202, 2013.

[50] S. Brischetto and E. Carrera, Coupled thermo-mechanical analysis of one-layered and multilayered isotropic and composite shells, *CMES: Computer Modeling in Engineering & Sciences*, 56, 249-301, 2010.

[51] S. Brischetto and E. Carrera, Coupled thermo-mechanical analysis of one-layered and multilayered plates, *Composite Structures*, 92, 1793-1812, 2010.

[52] S. Brischetto and E. Carrera, Coupled thermo-electro-mechanical analysis of smart plates embedding composite and piezoelectric layers, *Journal of Thermal Stresses*, 35, 766-804, 2012.

[53] M. Cho and J. Oh, Higher order zig-zag theory for fully coupled thermo-electric-mechanical smart composite plates, *International Journal of Solids and Structures*, 41, 1331-1356, 2004.

[54] A. Barut, E. Madenci and A. Tessler, Nonlinear thermoelastic analysis of composite panels under non-uniform temperature distribution, *International Journal of Solids and Structures*, 37, 3681-3713, 2000.

[55] K.N. Cho, A.G. Striz and C.W. Bert, Thermal stress analysis of laminate using higher-order theory in each layer, *Journal of Thermal Stresses*, 12, 321-332, 1989.

[56] J.N. Reddy and Y.S. Hsu, Effects of shear deformation and anisotropy on the thermal bending of layered composite plates, *Journal of Thermal Stresses*, 3, 475-493, 1980.

[57] M. Jafari, M.B. Nazari and A. Taherinasab, Thermal stress analysis in metallic plates with a non-circular hole subjected to uniform heat flux, *European Journal of Mechanics A/Solids*, 59, 356-363, 2016.

[58] L. Librescu and W. Lin, Non-linear response of laminated plates and shells to thermomechanical loading: implications of violation of interlaminar shear traction continuity requirement, *International Journal of Solids and Structures*, 36, 4111-4147, 1999.

[59] C.J. Miller, W.A. Millavec and T.P. Kicher, Thermal stress analysis of layered cylindrical shells, *AIAA Journal*, 19, 523-530, 1981.

[60] H.-S. Shen, Postbuckling of axially loaded FGM hybrid cylindrical shells in thermal environments, *Composites Science and Technology*, 65, 1675-1690, 2005.

[61] H.-S. Shen and N. Noda, Postbuckling of pressure-loaded FGM hybrid cylindrical shells in thermal environments, *Composite Structures*, 77, 546-560, 2007.

[62] H.-S. Shen and N. Noda, Postbuckling of FGM cylindrical shells under combined axial and radial mechanical loads in thermal environments, *International Journal of Solids and Structures*, 42, 4641-4662, 2005.

[63] Z.-Q. Cheng and R.C. Batra , Thermal effects on laminated composite shells containing interfacial imperfections, *Composite Structures*, 52, 3-11, 2001.

[64] M. Jabbari, M.Z. Nejad and M. Ghannad, Thermo-elastic analysis of axially functionally graded rotating thick truncated conical shells with varying thickness, *Composites. Part B: Engineering*, 96, 20-34, 2016.

[65] R. Rolfes and K. Rohwer, Integrated thermal and mechanical analysis of composite plates and shells, *Composites Science and Technology*, 60, 2097-2106, 2000.

[66] H. Santos, C.M. Mota Soares, C.A. Mota Soares and J.N. Reddy, A semi-analytical finite element model for the analysis of cylindrical shells made of functionally graded materials under thermal shock, *Composite Structures*, 86, 10-21, 2008.

[67] K. Daneshjoo and M. Ramezani, Coupled thermoelasticity in laminated composite plates based on Green-Lindsay model, *Composite Structures*, 55, 387-392, 2002.

[68] K. Daneshjoo and M. Ramezani, Classical coupled thermoelasticity in laminated composite plates based on third-order shear deformation theory, *Composite Structures*, 64, 369-375, 2004.

[69] A. Ibrahimbegovic, J.B. Colliat and L. Davenne, Thermomechanical coupling in folded plates and non-smooth shells, *Computer Methods in Applied Mechanics Engineering*, 194, 2686-2707, 2005.

[70] Z.-Y. Lee, Generalized coupled transient thermoelastic problem of multilayered hollow cylinder with hybrid boundary conditions, *International Communications in Heat and Mass Transfer*, 33, 518-528, 2006.

[71] J. Oh and M. Cho, A finite element based on cubic zig-zag plate theory for the prediction of thermo-electric-mechanical behaviors, *International Journal of Solids and Structures*, 41, 1357-1375, 2004.

[72] D. Holstein, P. Aswendt, R. Höfling, C.-D. Schmidt and W. Jüptner, Deformation analysis of thermally loaded composite tubes, *Composite Structures*, 40, 257-265, 1998.

[73] S. Brischetto, An exact 3D solution for free vibrations of multilayered cross-ply composite and sandwich plates and shells, *International Journal of Applied Mechanics*, 6, 1-42, 2014.

[74] S. Brischetto, Exact three-dimensional static analysis of single- and multi-layered plates and shells, *Composites. Part B: Engineering*, 119, 230-252, 2017.

[75] S. Brischetto, A closed-form 3D shell solution for multilayered structures subjected to different load combinations, *Aerospace Science and Technology*, 70, 29-46, 2017.

[76] S. Brischetto, Convergence analysis of the exponential matrix method for the solution of 3D equilibrium equations for free vibration analysis of plates and shells, *Composites. Part B: Engineering*, 98, 453-471, 2017.

[77] S. Brischetto and R. Torre, Convergence investigation for the exponential matrix and mathematical layers in the static analysis of multilayered composite structures, *Journal of Composites Science*, 1, 1-15, 2017.

[78] G.B. Arfken and H.J. Weber, Mathematical Methods for Physicists, Sixth Edition, Elsevier Academic Press, San Diego, USA, 2005.

[79] P.M. Morse and H. Feshbach, Methods of Theoretical Physics, McGraw-Hill, USA, 1953.

[80] M.N. Özişik, Heat Conduction, John Wiley & Sons, Inc., New York, 1993.

[81] Y. Povstenko, Fractional Thermoelasticity, Springer International Publishing, Switzerland, 2015.

[82] P. Moon and D.E. Spencer, Field Theory Handbook. Including Coordinate Systems, Differential Equations and Their Solutions, Springer-Verlag, Berlin, 1988.

[83] M.D. Mikhailov and M.N. Özişik, Unified Analysis and Solutions of Heat and Mass Diffusion, Dover Publications Inc., New York, 1984.

[84] W.E. Boyce and R.C. DiPrima, Elementary Differential Equations and Boundary Value Problems, John Wiley & Sons, Ltd., New York, 2001.

[85] Open document, Systems of Differential Equations, free available on http://www.math.utah.edu/gustafso/, accessed on 30th May 2013.

[86] A.W. Leissa, Vibration of Shells, NASA SP-288, Washington D.C., USA, 1973.

a/h	2	4	10	20	50	100
$\bar{w} = w/(a/h)^2$ at ($\alpha = a/2$, $\beta = b/2$, $z = +h/2$)						
Ref.(θ_a) [12]	96.79	42.69	17.39	12.12	10.50	10.26
$M = 102$						
3D(θ_a)	97.02	42.69	17.39	12.12	10.50	10.26
3D(θ_c,1D)	97.02	42.69	17.39	12.12	10.50	10.26
3D(θ_c,3D)	49.06	32.12	16.40	11.93	10.47	10.25
$M = 210$						
3D(θ_a)	96.82	42.69	17.39	12.12	10.50	10.26
3D(θ_c,1D)	96.82	42.69	17.39	12.12	10.50	10.26
3D(θ_c,3D)	48.88	32.12	16.39	11.93	10.47	10.25
$M = 300$						
3D(θ_a)	96.80	42.69	17.39	12.12	10.50	10.26
3D(θ_c,1D)	96.80	42.69	17.39	12.12	10.50	10.26
3D(θ_c,3D)	48.87	32.12	16.39	11.93	10.47	10.25
$\sigma_{\alpha\alpha}$ at ($\alpha = a/2$, $\beta = b/2$, $z = +h/2$)						
Ref.(θ_a) [12]	1390	1183	1026	982.0	967.5	965.4
$M = 102$						
3D(θ_a)	1123	1183	1026	982.0	967.5	965.4
3D(θ_c,1D)	1123	1183	1026	982.0	967.5	965.4
3D(θ_c,3D)	299.0	796.8	948.0	961.8	964.3	964.5
$M = 210$						
3D(θ_a)	1359	1183	1026	982.0	967.5	965.4
3D(θ_c,1D)	1359	1183	1026	982.0	967.5	965.4
3D(θ_c,3D)	473.0	796.8	948.0	961.8	964.3	964.5
$M = 300$						
3D(θ_a)	1379	1183	1026	982.0	967.5	965.4
3D(θ_c,1D)	1379	1183	1026	982.0	967.5	965.4
3D(θ_c,3D)	487.6	796.8	948.0	961.8	964.3	964.5
$\sigma_{\alpha\beta}$ at ($\alpha = 0$, $\beta = 0$, $z = -h/2$)						
Ref.(θ_a) [12]	269.3	157.0	76.29	57.35	51.41	50.53
$M = 102$						
3D(θ_a)	269.3	157.0	76.29	57.35	51.41	50.53
3D(θ_c,1D)	269.3	157.0	76.29	57.35	51.41	50.53
3D(θ_c,3D)	143.0	119.4	71.96	56.46	51.27	50.50
$M = 210$						
3D(θ_a)	269.3	157.0	76.29	57.35	51.41	50.53
3D(θ_c,1D)	269.3	157.0	76.29	57.35	51.41	50.53
3D(θ_c,3D)	142.9	119.4	71.96	56.46	51.27	50.50
$M = 300$						
3D(θ_a)	269.3	157.0	76.29	57.35	51.41	50.53
3D(θ_c,1D)	269.3	157.0	76.29	57.35	51.41	50.53
3D(θ_c,3D)	142.9	119.4	71.96	56.46	51.27	50.50

Table 1: First assessment, $0°/90°/0°$ composite plate with external sovra-temperature amplitudes $\Theta_t = +1K$ and $\Theta_b = -1K$ (m=n=1). Reference solution (Ref.) is the 3D thermo-elastic model by Bhaskar et al. [12] based on an assumed linear temperature profile though the thickness (θ_a). Proposed 3D thermo-elastic solution uses order $N = 3$ for the exponential matrix and different M mathematical layers.

R_α/h	5	10	50	100	1000
$w[mm]$ at ($\alpha = a/2$, $\beta = b/2$, $z = 0$)					
Ref.(θ_a) [50]	0.007	0.0011	0.0048	0.0117	0.0634
Ref.(θ_M) [50]	0.002	0.0010	0.0060	0.0129	0.0424
$M = 100$					
3D(θ_a)	0.007	0.0011	0.0048	0.0117	0.0634
3D(θ_c,1D)	0.002	0.0010	0.0060	0.0129	0.0424
3D(θ_c,3D)	0.002	0.0010	0.0060	0.0129	0.0424
$M = 200$					
3D(θ_a)	0.007	0.0011	0.0048	0.0117	0.0634
3D(θ_c,1D)	0.002	0.0010	0.0060	0.0129	0.0424
3D(θ_c,3D)	0.002	0.0010	0.0060	0.0129	0.0424
$M = 300$					
3D(θ_a)	0.007	0.0011	0.0048	0.0117	0.0634
3D(θ_c,1D)	0.002	0.0010	0.0060	0.0129	0.0424
3D(θ_c,3D)	0.002	0.0010	0.0060	0.0129	0.0424
$u[10^{-4}m]$ at ($\alpha = 0$, $\beta = b/2$, $z = +h/2$)					
Ref.(θ_a) [50]	-0.0052	-0.0045	-0.0035	-0.0033	0.0010
Ref.(θ_M) [50]	-0.0031	-0.0031	-0.0027	-0.0023	0.0009
$M = 100$					
3D(θ_a)	-0.0053	-0.0045	-0.0035	-0.0033	0.0010
3D(θ_c,1D)	-0.0046	-0.0037	-0.0027	-0.0023	0.0009
3D(θ_c,3D)	-0.0031	-0.0031	-0.0027	-0.0023	0.0009
$M = 200$					
3D(θ_a)	-0.0052	-0.0045	-0.0035	-0.0033	0.0010
3D(θ_c,1D)	-0.0046	-0.0037	-0.0027	-0.0023	0.0009
3D(θ_c,3D)	-0.0031	-0.0031	-0.0027	-0.0023	0.0009
$M = 300$					
3D(θ_a)	-0.0052	-0.0045	-0.0035	-0.0033	0.0010
3D(θ_c,1D)	-0.0046	-0.0037	-0.0027	-0.0023	0.0009
3D(θ_c,3D)	-0.0031	-0.0031	-0.0027	-0.0023	0.0009

Table 2: Second assessment, two-layered isotropic cylindrical shell with external sovra-temperature amplitudes $\Theta_t = +1K$ and $\Theta_b = 0K$ (m=n=1). Reference solutions (Ref.) are the quasi-3D layer wise models in Brischetto and Carrera [50] based on an assumed linear temperature profile though the thickness (θ_a) or on a fully-coupled thermo-elastic theory with modelled temperature field (θ_M). Proposed 3D thermo-elastic solution uses order $N = 3$ for the exponential matrix and different M mathematical layers.

R_α/h	50	100	500
$\bar{w} = \frac{10h}{b^2\mu_1 T_1} w$ at ($\alpha = a/2$, $\beta = b/2$, $z = 0$)			
Ref.(θ_a) [36]	1.0588	1.1256	1.1487
$M = 100$			
3D(θ_a)	1.0570	1.1237	1.1467
3D(θ_c,1D)	1.0570	1.1237	1.1467
3D(θ_c,3D)	1.0142	1.0780	1.1000
$M = 200$			
3D(θ_a)	1.0570	1.1237	1.1467
3D(θ_c,1D)	1.0570	1.1237	1.1467
3D(θ_c,3D)	1.0142	1.0780	1.1000
$M = 300$			
3D(θ_a)	1.0570	1.1237	1.1467
3D(θ_c,1D)	1.0570	1.1237	1.1467
3D(θ_c,3D)	1.0142	1.0780	1.1000

Table 3: Third assessment, $0^\circ/90^\circ$ composite spherical shell with external sovra-temperature amplitudes $\Theta_t = +0.5K$ and $\Theta_b = -0.5K$ (m=n=1). Reference solution (Ref.) is the exact higher order 2D thermo-elastic model by Khare et al. [36] based on an assumed linear temperature profile though the thickness (θ_a). Proposed 3D thermo-elastic solution uses order $N = 3$ for the exponential matrix and different M mathematical layers.

a/h	2	5	10	20	50	100
u[10^{-5}m] at ($\alpha = 0$, $\beta = b/2$, $z = +h/2$)						
3D(θ_a)	-0.0729	-0.1661	-0.3297	-0.6583	-1.6450	-3.2898
3D(θ_c,1D)	-0.0729	-0.1661	-0.3297	-0.6583	-1.6450	-3.2898
3D(θ_c,3D)	-0.0369	-0.1351	-0.3104	-0.6480	-1.6408	-3.2877
v[10^{-5}m] at ($\alpha = a/2$, $\beta = 0$, $z = -h/2$)						
3D(θ_a)	0.5261	0.5861	0.5918	0.7981	1.7020	3.3184
3D(θ_c,1D)	0.5261	0.5861	0.5918	0.7981	1.7020	3.3184
3D(θ_c,3D)	0.2718	0.4771	0.5572	0.7856	1.6977	3.3162
w[10^{-5}m] at ($\alpha = a/2$, $\beta = b/2$, $z = 0$)						
3D(θ_a)	0.0936	0.7345	2.3955	8.7090	52.699	209.77
3D(θ_c,1D)	0.0936	0.7345	2.3955	8.7090	52.699	209.77
3D(θ_c,3D)	0.0958	0.6221	2.2634	8.5750	52.565	209.64
$\sigma_{\alpha\alpha}$[10^4Pa] at ($\alpha = a/2$, $\beta = b/2$, $z = +h/2$)						
3D(θ_a)	13.240	10.687	10.238	10.105	10.065	10.059
3D(θ_c,1D)	13.240	10.687	10.238	10.105	10.065	10.059
3D(θ_c,3D)	2.7489	7.2060	9.1706	9.8214	10.019	10.047
$\sigma_{\beta\beta}$[10^4Pa] at ($\alpha = a/2$, $\beta = b/2$, $z = -h/2$)						
3D(θ_a)	6.4558	9.6469	10.911	11.331	11.458	11.477
3D(θ_c,1D)	6.4558	9.6469	10.911	11.331	11.458	11.477
3D(θ_c,3D)	9.3207	10.155	10.997	11.347	11.461	11.478
$\sigma_{\alpha\beta}$[10^4Pa] at ($\alpha = 0$, $\beta = 0$, $z = +h/4$)						
3D(θ_a)	-1.4933	-0.8115	-0.5003	-0.3950	-0.3628	-0.3581
3D(θ_c,1D)	-1.4933	-0.8115	-0.5003	-0.3950	-0.3628	-0.3581
3D(θ_c,3D)	-0.6148	-0.6468	-0.4205	-0.3887	-0.3619	-0.3579
$\sigma_{\alpha z}$[10^4Pa] at ($\alpha = 0$, $\beta = b/2$, $z = +h/4$)						
3D(θ_a)	1.0518	0.9566	0.5860	0.3108	0.1265	0.0634
3D(θ_c,1D)	1.0518	0.9566	0.5860	0.3108	0.1265	0.0634
3D(θ_c,3D)	0.5278	0.7701	0.5501	0.3057	0.1261	0.0633
$\sigma_{\beta z}$[10^4Pa] at ($\alpha = a/2$, $\beta = 0$, $z = -h/4$)						
3D(θ_a)	-1.0666	-0.9325	-0.5815	-0.3101	-0.1264	-0.0634
3D(θ_c,1D)	-1.0666	-0.9325	-0.5815	-0.3101	-0.1264	-0.0634
3D(θ_c,3D)	-0.5417	-0.7727	-0.5500	-0.3056	-0.1261	-0.0633
σ_{zz}[Pa] at ($\alpha = a/2$, $\beta = b/2$, $z = -h/4$)						
3D(θ_a)	1955.6	136.85	11.229	0.7601	0.0199	0.0013
3D(θ_c,1D)	1955.6	136.85	11.229	0.7601	0.0199	0.0013
3D(θ_c,3D)	-503.79	-10.923	0.4205	0.0598	0.0018	0.0001

Table 4: First benchmark, simply-supported one-layered 0° composite square plate with external sovra-temperature amplitudes $\Theta_t = +0.5K$ and $\Theta_b = -0.5K$ ($m = n = 1$). Proposed 3D thermo-elastic solution uses order $N = 3$ for the exponential matrix and $M = 300$ mathematical layers.

a/h	2	5	10	20	50	100
u[10^{-5}m] at ($\alpha = 0$, $\beta = b/2$, $z = +h/2$)						
3D(θ_a)	-0.0791	-0.1779	-0.3388	-0.6635	-1.6472	-3.2909
3D(θ_c,1D)	-0.0791	-0.1779	-0.3388	-0.6635	-1.6472	-3.2909
3D(θ_c,3D)	-0.0400	-0.1451	-0.3191	-0.6532	-1.6430	-3.2888
v[10^{-5}m] at ($\alpha = a/2$, $\beta = 0$, $z = -h/2$)						
3D(θ_a)	0.4834	0.5408	0.5747	0.7919	1.6999	3.3173
3D(θ_c,1D)	0.4834	0.5408	0.5747	0.7919	1.6999	3.3173
3D(θ_c,3D)	0.2610	0.4471	0.5426	0.7798	1.6956	3.3152
w[10^{-5}m] at ($\alpha = a/2$, $\beta = b/2$, $z = 0$)						
3D(θ_a)	0.1159	0.8948	2.6731	9.0380	53.045	210.12
3D(θ_c,1D)	0.1159	0.8948	2.6731	9.0380	53.045	210.12
3D(θ_c,3D)	0.1132	0.7622	2.5294	8.9002	52.910	209.99
$\sigma_{\alpha\alpha}$[10^4Pa] at ($\alpha = a/2$, $\beta = b/2$, $z = +h/2$)						
3D(θ_a)	14.818	11.928	10.728	10.246	10.088	10.065
3D(θ_c,1D)	14.818	11.928	10.728	10.246	10.088	10.065
3D(θ_c,3D)	3.5819	8.2513	9.6365	9.9607	10.042	10.053
$\sigma_{\beta\beta}$[10^4Pa] at ($\alpha = a/2$, $\beta = b/2$, $z = -h/2$)						
3D(θ_a)	6.9043	9.8311	10.943	11.336	11.459	11.477
3D(θ_c,1D)	6.9043	9.8311	10.943	11.336	11.459	11.477
3D(θ_c,3D)	9.4299	10.275	11.024	11.352	11.461	11.478
$\sigma_{\alpha\beta}$[10^4Pa] at ($\alpha = 0$, $\beta = 0$, $z = +h/4$)						
3D(θ_a)	-1.0256	-0.6194	-0.4439	-0.3805	-0.3605	-0.3575
3D(θ_c,1D)	-1.0256	-0.6194	-0.4439	-0.3805	-0.3605	-0.3575
3D(θ_c,3D)	0.4520	-0.5005	-0.4177	-0.3745	-0.3596	-0.3573
$\sigma_{\alpha z}$[10^4Pa] at ($\alpha = 0$, $\beta = b/2$, $z = +h/4$)						
3D(θ_a)	1.1161	0.9225	0.5754	0.3091	0.1263	0.0634
3D(θ_c,1D)	1.1161	0.9225	0.5754	0.3091	0.1263	0.0634
3D(θ_c,3D)	0.5190	0.7375	0.5398	0.3040	0.1260	0.0633
$\sigma_{\beta z}$[10^4Pa] at ($\alpha = a/2$, $\beta = 0$, $z = -h/4$)						
3D(θ_a)	-1.3762	-0.9939	-0.5889	-0.3110	-0.1265	-0.0634
3D(θ_c,1D)	-1.3762	-0.9939	-0.5889	-0.3110	-0.1265	-0.0634
3D(θ_c,3D)	-0.6537	-0.8164	-0.5567	-0.3065	-0.1262	-0.0633
σ_{zz}[Pa] at ($\alpha = a/2$, $\beta = b/2$, $z = -h/4$)						
3D(θ_a)	1704.4	124.34	11.042	0.7725	0.0205	0.0013
3D(θ_c,1D)	1704.4	124.34	11.042	0.7725	0.0205	0.0013
3D(θ_c,3D)	-512.45	-16.459	0.3721	0.0744	0.0024	0.0002

Table 5: Second benchmark, simply-supported three-layered $0°/90°/0°$ composite square plate with external sovra-temperature amplitudes $\Theta_t = +0.5K$ and $\Theta_b = -0.5K$ ($m = n = 1$). Proposed 3D thermo-elastic solution uses order $N = 3$ for the exponential matrix and $M = 300$ mathematical layers.

R_α/h	2	5	10	20	50	100
u[10^{-5}m] at ($\alpha = 0$, $\beta = b/2$, $z = +h/2$)						
3D(θ_a)	3.0170	1.8209	0.9969	0.5167	0.2105	0.1059
3D(θ_c,1D)	3.0170	1.8209	0.9969	0.5167	0.2105	0.1059
3D(θ_c,3D)	3.0032	1.8196	0.9967	0.5167	0.2105	0.1059
v[10^{-5}m] at ($\alpha = a/2$, $\beta = 0$, $z = -h/2$)						
3D(θ_a)	0.9712	-0.1470	-0.1879	-0.1232	-0.0563	-0.0293
3D(θ_c,1D)	0.9712	-0.1470	-0.1879	-0.1232	-0.0563	-0.0293
3D(θ_c,3D)	0.9488	-0.1481	-0.1880	-0.1232	-0.0563	-0.0293
w[10^{-5}m] at ($\alpha = a/2$, $\beta = b/2$, $z = 0$)						
3D(θ_a)	4.7030	2.3414	1.2126	0.6117	0.2453	0.1227
3D(θ_c,1D)	4.7030	2.3414	1.2126	0.6117	0.2453	0.1227
3D(θ_c,3D)	4.7108	2.3416	1.2126	0.6117	0.2453	0.1227
$\sigma_{\alpha\alpha}$[10^4Pa] at ($\alpha = a/2$, $\beta = b/2$, $z = +h/2$)						
3D(θ_a)	-93.780	-115.72	-123.27	-126.90	-128.99	-129.68
3D(θ_c,1D)	-93.780	-115.72	-123.27	-126.90	-128.99	-129.68
3D(θ_c,3D)	-93.790	-115.72	-123.27	-126.90	-128.99	-129.68
$\sigma_{\beta\beta}$[10^4Pa] at ($\alpha = a/2$, $\beta = b/2$, $z = -h/2$)						
3D(θ_a)	128.80	134.91	133.67	132.27	131.19	130.78
3D(θ_c,1D)	128.80	134.91	133.67	132.27	131.19	130.78
3D(θ_c,3D)	128.97	134.91	133.67	132.27	131.19	130.78
$\sigma_{\alpha\beta}$[10^4Pa] at ($\alpha = 0$, $\beta = 0$, $z = +h/4$)						
3D(θ_a)	4.3550	3.4394	2.0110	1.0738	0.4451	0.2250
3D(θ_c,1D)	4.3550	3.4394	2.0110	1.0738	0.4451	0.2250
3D(θ_c,3D)	4.2954	3.4341	2.0102	1.0737	0.4451	0.2250
$\sigma_{\alpha z}$[10^4Pa] at ($\alpha = 0$, $\beta = b/2$, $z = +h/4$)						
3D(θ_a)	-8.4089	-4.3683	-2.3272	-1.1947	-0.4846	-0.2434
3D(θ_c,1D)	-8.4089	-4.3683	-2.3272	-1.1947	-0.4846	-0.2434
3D(θ_c,3D)	-8.3275	-4.3624	-2.3264	-1.1946	-0.4846	-0.2434
$\sigma_{\beta z}$[10^4Pa] at ($\alpha = a/2$, $\beta = 0$, $z = -h/4$)						
3D(θ_a)	-9.8045	-4.9447	-2.5480	-1.2810	-0.5125	-0.2561
3D(θ_c,1D)	-9.8045	-4.9447	-2.5480	-1.2810	-0.5125	-0.2561
3D(θ_c,3D)	-9.7151	-4.9382	-2.5472	-1.2809	-0.5125	-0.2561
σ_{zz}[10^4Pa] at ($\alpha = a/2$, $\beta = b/2$, $z = -h/4$)						
3D(θ_a)	14.109	5.3127	2.5599	1.2521	0.4937	0.2456
3D(θ_c,1D)	14.109	5.3127	2.5599	1.2521	0.4937	0.2456
3D(θ_c,3D)	13.978	5.3055	2.5591	1.2520	0.4937	0.2456

Table 6: Third benchmark, simply-supported one-layered isotropic Al2024 cylinder with external sovra-temperature amplitudes $\Theta_t = +0.5K$ and $\Theta_b = -0.5K$ ($m = 2$ and $n = 1$). Proposed 3D thermo-elastic solution uses order $N = 3$ for the exponential matrix and $M = 300$ mathematical layers.

R_α/h	2	5	10	20	50	100
u[10^{-5}m] at ($\alpha = 0$, $\beta = b/2$, $z = +h/2$)						
3D(θ_a)	1.2933	0.2640	-0.3392	-0.6804	-0.8952	-0.9683
3D(θ_c,1D)	0.3491	-1.5604	-2.4805	-2.9740	-3.2766	-3.3783
3D(θ_c,3D)	0.4135	-1.5375	-2.4736	-2.9721	-3.2763	-3.3782
v[10^{-5}m] at ($\alpha = a/2$, $\beta = 0$, $z = -h/2$)						
3D(θ_a)	1.4618	0.8157	0.8649	0.9555	1.0315	1.0604
3D(θ_c,1D)	2.9972	2.7826	3.1004	3.3448	3.5181	3.5802
3D(θ_c,3D)	2.8572	2.7563	3.0931	3.3429	3.5178	3.5801
w[10^{-5}m] at ($\alpha = a/2$, $\beta = b/2$, $z = 0$)						
3D(θ_a)	0.9037	-0.6784	-1.4092	-1.7945	-2.0284	-2.1065
3D(θ_c,1D)	-3.1677	-5.4294	-6.3630	-6.8341	-7.1132	-7.2051
3D(θ_c,3D)	-2.8414	-5.3676	-6.3469	-6.8300	-7.1125	-7.2050
$\sigma_{\alpha\alpha}$[10^4Pa] at ($\alpha = a/2$, $\beta = b/2$, $z = +h/2$)						
3D(θ_a)	-60.434	-77.267	-82.907	-85.559	-87.072	-87.561
3D(θ_c,1D)	-103.96	-121.98	-127.17	-129.39	-130.57	-130.94
3D(θ_c,3D)	-100.49	-121.39	-127.02	-129.35	-130.57	-130.94
$\sigma_{\beta\beta}$[10^4Pa] at ($\alpha = a/2$, $\beta = b/2$, $z = -h/2$)						
3D(θ_a)	121.30	123.62	121.82	120.33	119.24	118.85
3D(θ_c,1D)	105.78	102.14	97.324	94.173	92.057	91.316
3D(θ_c,3D)	107.14	102.42	97.404	94.195	92.061	91.317
$\sigma_{\alpha\beta}$[10^4Pa] at ($\alpha = 0$, $\beta = 0$, $z = +h/4$)						
3D(θ_a)	5.7913	3.8577	2.1752	1.1434	0.4698	0.2369
3D(θ_c,1D)	9.9534	5.7771	3.1362	1.6193	0.6583	0.3308
3D(θ_c,3D)	9.5595	5.7469	3.1324	1.6188	0.6583	0.3308
$\sigma_{\alpha z}$[10^4Pa] at ($\alpha = 0$, $\beta = b/2$, $z = +h/4$)						
3D(θ_a)	-6.2364	-3.2046	-1.6959	-0.8672	-0.3509	-0.1760
3D(θ_c,1D)	-10.571	-4.8990	-2.5119	-1.2649	-0.5072	-0.2537
3D(θ_c,3D)	-10.179	-4.8738	-2.5088	-1.2645	-0.5072	-0.2537
$\sigma_{\beta z}$[10^4Pa] at ($\alpha = a/2$, $\beta = 0$, $z = -h/4$)						
3D(θ_a)	-9.4212	-4.4541	-2.2626	-1.1307	-0.4509	-0.2251
3D(θ_c,1D)	-10.034	-4.5094	-2.2221	-1.0907	-0.4298	-0.2137
3D(θ_c,3D)	-9.8714	-4.5011	-2.2213	-1.0906	-0.4298	-0.2137
σ_{zz}[10^4Pa] at ($\alpha = a/2$, $\beta = b/2$, $z = -h/4$)						
3D(θ_a)	12.392	4.6425	2.2412	1.0977	0.4333	0.2156
3D(θ_c,1D)	13.659	4.7199	2.2012	1.0583	0.4129	0.2047
3D(θ_c,3D)	13.403	4.7109	2.2004	1.0582	0.4129	0.2047

Table 7: Fourth benchmark, simply-supported two-layered isotropic Al2024/Ti22 cylinder with external sovra-temperature amplitudes $\Theta_t = +0.5K$ and $\Theta_b = -0.5K$ ($m = 2$ and $n = 1$). Proposed 3D thermo-elastic solution uses order $N = 3$ for the exponential matrix and $M = 300$ mathematical layers.

R_α/h	2	5	10	20	50	100
u[10^{-5}m] at ($\alpha=0$, $\beta=b/2$, $z=+h/2$)						
3D(θ_a)	-3.5730	-1.7728	0.6652	5.4209	19.623	43.275
3D(θ_c,1D)	-3.5730	-1.7728	0.6652	5.4209	19.623	43.275
3D(θ_c,3D)	-3.2200	-1.7140	0.6772	5.4223	19.622	43.274
v[10^{-5}m] at ($\alpha=a/2$, $\beta=0$, $z=-h/2$)						
3D(θ_a)	0.0000	0.0000	0.0000	0.0000	0.0000	0.0000
3D(θ_c,1D)	0.0000	0.0000	0.0000	0.0000	0.0000	0.0000
3D(θ_c,3D)	0.0000	0.0000	0.0000	0.0000	0.0000	0.0000
w[10^{-5}m] at ($\alpha=a/2$, $\beta=b/2$, $z=0$)						
3D(θ_a)	2.0687	6.3251	13.444	27.651	70.233	141.18
3D(θ_c,1D)	2.0687	6.3251	13.444	27.651	70.233	141.18
3D(θ_c,3D)	2.1059	6.3144	13.431	27.642	70.229	141.18
$\sigma_{\alpha\alpha}$[10^4Pa] at ($\alpha=a/2$, $\beta=b/2$, $z=+h/2$)						
3D(θ_a)	7.0586	0.0892	-0.5280	-0.4182	-0.2053	-0.1117
3D(θ_c,1D)	7.0586	0.0892	-0.5280	-0.4182	-0.2053	-0.1117
3D(θ_c,3D)	-5.0098	-2.1901	-1.1261	-0.5712	-0.2301	-0.1179
$\sigma_{\beta\beta}$[10^4Pa] at ($\alpha=a/2$, $\beta=b/2$, $z=-h/2$)						
3D(θ_a)	1.5486	-0.2240	-0.2448	-0.1544	-0.0694	-0.0351
3D(θ_c,1D)	1.5486	-0.2240	-0.2448	-0.1544	-0.0694	-0.0351
3D(θ_c,3D)	-1.7924	-0.7635	-0.3792	-0.1879	-0.0747	-0.0364
$\sigma_{\alpha\beta}$[10^4Pa] at ($\alpha=0$, $\beta=0$, $z=+h/4$)						
3D(θ_a)	0.0000	0.0000	0.0000	0.0000	0.0000	0.0000
3D(θ_c,1D)	0.0000	0.0000	0.0000	0.0000	0.0000	0.0000
3D(θ_c,3D)	0.0000	0.0000	0.0000	0.0000	0.0000	0.0000
$\sigma_{\alpha z}$[10^4Pa] at ($\alpha=0$, $\beta=b/2$, $z=+h/4$)						
3D(θ_a)	0.8436	-0.0115	-0.0174	-0.6241×10^{-2}	-0.1177×10^{-2}	-0.0324×10^{-2}
3D(θ_c,1D)	0.8436	-0.0115	-0.0174	-0.6241×10^{-2}	-0.1177×10^{-2}	-0.0324×10^{-2}
3D(θ_c,3D)	-66.928	-0.1246	-0.0321	-0.8098×10^{-2}	-0.1297×10^{-2}	-0.0339×10^{-2}
$\sigma_{\beta z}$[10^4Pa] at ($\alpha=a/2$, $\beta=0$, $z=-h/4$)						
3D(θ_a)	0.0000	0.0000	0.0000	0.0000	0.0000	0.0000
3D(θ_c,1D)	0.0000	0.0000	0.0000	0.0000	0.0000	0.0000
3D(θ_c,3D)	0.0000	0.0000	0.0000	0.0000	0.0000	0.0000
σ_{zz}[Pa] at ($\alpha=a/2$, $\beta=b/2$, $z=-h/4$)						
3D(θ_a)	346.96	-27.698	-51.184	-19.624	-3.8665	-0.9796
3D(θ_c,1D)	346.96	-27.698	-51.184	-19.624	-3.8665	-0.9796
3D(θ_c,3D)	14.887	-285.50	-91.627	-25.148	-4.2371	-1.0266

Table 8: Fifth benchmark, simply-supported one-layered Ti22 isotropic cylindrical shell with external sovra-temperature amplitudes $\Theta_t = 1.0K$ and $\Theta_b = 0.0K$ ($m = 1$ and $n = 0$). Proposed 3D thermo-elastic solution uses order $N = 3$ for the exponential matrix and $M = 300$ mathematical layers.

R_α/h	2	5	10	20	50	100
u[10^{-5}m] at ($\alpha = 0$, $\beta = b/2$, $z = +h/2$)						
3D(θ_a)	-10.134	-6.2106	0.7010	14.818	57.457	128.61
3D(θ_c,1D)	-10.547	-6.0658	1.7093	17.534	65.279	144.94
3D(θ_c,3D)	-10.428	-6.0160	1.7227	17.536	65.279	144.94
v[10^{-5}m] at ($\alpha = a/2$, $\beta = 0$, $z = -h/2$)						
3D(θ_a)	0.0000	0.0000	0.0000	0.0000	0.0000	0.0000
3D(θ_c,1D)	0.0000	0.0000	0.0000	0.0000	0.0000	0.0000
3D(θ_c,3D)	0.0000	0.0000	0.0000	0.0000	0.0000	0.0000
w[10^{-5}m] at ($\alpha = a/2$, $\beta = b/2$, $z = 0$)						
3D(θ_a)	2.8059	15.568	37.159	80.036	208.30	421.89
3D(θ_c,1D)	3.0068	17.794	42.099	90.160	233.78	472.91
3D(θ_c,3D)	3.4353	17.879	42.112	90.159	233.78	472.90
$\sigma_{\alpha\alpha}$[10^4Pa] at ($\alpha = a/2$, $\beta = b/2$, $z = +h/2$)						
3D(θ_a)	40.943	30.197	28.954	28.961	29.193	29.302
3D(θ_c,1D)	57.526	46.613	45.332	45.332	45.565	45.674
3D(θ_c,3D)	50.807	45.457	45.031	45.255	45.553	45.671
$\sigma_{\beta\beta}$[10^4Pa] at ($\alpha = a/2$, $\beta = b/2$, $z = -h/2$)						
3D(θ_a)	11.276	5.8276	5.0898	4.8953	4.8300	4.8193
3D(θ_c,1D)	6.0584	0.8660	0.1630	-0.0221	-0.0839	-0.0936
3D(θ_c,3D)	3.7887	0.6018	0.1018	-0.0369	-0.0863	-0.0941
$\sigma_{\alpha\beta}$[10^4Pa] at ($\alpha = 0$, $\beta = 0$, $z = +h/4$)						
3D(θ_a)	0.0000	0.0000	0.0000	0.0000	0.0000	0.0000
3D(θ_c,1D)	0.0000	0.0000	0.0000	0.0000	0.0000	0.0000
3D(θ_c,3D)	0.0000	0.0000	0.0000	0.0000	0.0000	0.0000
$\sigma_{\alpha z}$[10^4Pa] at ($\alpha = 0$, $\beta = b/2$, $z = +h/4$)						
3D(θ_a)	2.4049	0.8769	0.4277	0.2118	0.0843	0.0421
3D(θ_c,1D)	2.3775	0.8540	0.4130	0.2036	0.0808	0.0403
3D(θ_c,3D)	1.8442	0.8126	0.4077	0.2029	0.0808	0.0403
$\sigma_{\beta z}$[10^4Pa] at ($\alpha = a/2$, $\beta = 0$, $z = -h/4$)						
3D(θ_a)	0.0000	0.0000	0.0000	0.0000	0.0000	0.0000
3D(θ_c,1D)	0.0000	0.0000	0.0000	0.0000	0.0000	0.0000
3D(θ_c,3D)	0.0000	0.0000	0.0000	0.0000	0.0000	0.0000
σ_{zz}[10^4Pa] at ($\alpha = a/2$, $\beta = b/2$, $z = -h/4$)						
3D(θ_a)	-22.828	0.1782	0.1182	0.0657	0.0278	0.0142
3D(θ_c,1D)	-728.70	0.2087	0.1288	0.0698	0.0292	0.0148
3D(θ_c,3D)	-273.08	0.2005	0.1273	0.0696	0.0292	0.0148

Table 9: Sixth benchmark, simply-supported sandwich Al2024/PVC/Al2024 cylindrical shell with external sovra-temperature amplitudes $\Theta_t = 1.0K$ and $\Theta_b = 0.0K$ ($m = 1$ and $n = 0$). Proposed 3D thermo-elastic solution uses order $N = 3$ for the exponential matrix and $M = 300$ mathematical layers.

R_α/h	2	5	10	20	50	100
u[10^{-5}m] at ($\alpha = 0$, $\beta = b/2$, $z = +h/2$)						
3D(θ_a)	-2.9176	-1.7996	-0.8976	-0.3635	-0.1096	-0.0478
3D(θ_c,1D)	-2.9176	-1.7996	-0.8976	-0.3635	-0.1096	-0.0478
3D(θ_c,3D)	-2.4554	-1.7161	-0.8837	-0.3617	-0.1095	-0.0478
v[10^{-5}m] at ($\alpha = a/2$, $\beta = 0$, $z = -h/2$)						
3D(θ_a)	0.6033	1.3064	1.0998	0.6572	0.2771	0.1394
3D(θ_c,1D)	0.6033	1.3064	1.0998	0.6572	0.2771	0.1394
3D(θ_c,3D)	0.7619	1.2903	1.0921	0.6558	0.2770	0.1394
w[10^{-5}m] at ($\alpha = a/2$, $\beta = b/2$, $z = 0$)						
3D(θ_a)	2.5188	5.1544	6.5432	6.7022	6.3930	6.2141
3D(θ_c,1D)	2.5188	5.1544	6.5432	6.7022	6.3930	6.2141
3D(θ_c,3D)	2.1970	4.9750	6.4703	6.6807	6.3894	6.2132
$\sigma_{\alpha\alpha}$[10^4Pa] at ($\alpha = a/2$, $\beta = b/2$, $z = +h/2$)						
3D(θ_a)	-26.340	-45.030	-81.526	-124.05	-157.00	-168.52
3D(θ_c,1D)	-26.340	-45.030	-81.526	-124.05	-157.00	-168.52
3D(θ_c,3D)	-76.934	-57.708	-84.933	-124.86	-157.12	-168.55
$\sigma_{\beta\beta}$[10^4Pa] at ($\alpha = a/2$, $\beta = b/2$, $z = -h/2$)						
3D(θ_a)	-11.391	31.845	99.865	144.84	168.36	174.67
3D(θ_c,1D)	-11.391	31.845	99.865	144.84	168.36	174.67
3D(θ_c,3D)	-26.667	28.711	98.425	144.33	168.26	174.65
$\sigma_{\alpha\beta}$[10^4Pa] at ($\alpha = 0$, $\beta = 0$, $z = +h/4$)						
3D(θ_a)	-63.025	-43.070	-17.981	-5.0090	-0.6002	-0.0429
3D(θ_c,1D)	-63.025	-43.070	-17.981	-5.0090	-0.6002	-0.0429
3D(θ_c,3D)	-50.132	-40.541	-17.589	-4.9637	-0.5977	-0.0426
$\sigma_{\alpha z}$[10^4Pa] at ($\alpha = 0$, $\beta = b/2$, $z = +h/4$)						
3D(θ_a)	16.767	3.5155	-2.2579	-3.0027	-1.7068	-0.9349
3D(θ_c,1D)	16.767	3.5155	-2.2579	-3.0027	-1.7068	-0.9349
3D(θ_c,3D)	6.5367	2.3933	-2.3892	-3.0150	-1.7074	-0.9350
$\sigma_{\beta z}$[10^4Pa] at ($\alpha = a/2$, $\beta = 0$, $z = -h/4$)						
3D(θ_a)	14.469	4.0791	-2.4801	-3.1541	-1.7412	-0.9443
3D(θ_c,1D)	14.469	4.0791	-2.4801	-3.1541	-1.7412	-0.9443
3D(θ_c,3D)	15.652	3.9491	-2.4699	-3.1478	-1.7406	-0.9442
σ_{zz}[10^4Pa] at ($\alpha = a/2$, $\beta = b/2$, $z = -h/4$)						
3D(θ_a)	1.4441	2.9960	3.6512	2.6452	1.2471	0.6508
3D(θ_c,1D)	1.4441	2.9960	3.6512	2.6452	1.2471	0.6508
3D(θ_c,3D)	4.8006	3.0618	3.6338	2.6400	1.2466	0.6507

Table 10: Seventh benchmark, simply-supported one-layered isotropic Steel spherical shell with external sovra-temperature amplitudes $\Theta_t = 1.0K$ and $\Theta_b = 0.0K$ ($m = n = 1$). Proposed 3D thermo-elastic solution uses order $N = 3$ for the exponential matrix and $M = 300$ mathematical layers.

R_α/h	2	5	10	20	50	100
u[10^{-5}m] at ($\alpha = 0$, $\beta = b/2$, $z = +h/2$)						
3D(θ_a)	-2.7765	-1.6822	-0.8444	-0.3527	-0.1118	-0.0502
3D(θ_c,1D)	-2.8569	-1.6278	-0.7481	-0.2799	-0.0771	-0.0320
3D(θ_c,3D)	-2.5560	-1.5832	-0.7414	-0.2791	-0.0771	-0.0320
v[10^{-5}m] at ($\alpha = a/2$, $\beta = 0$, $z = -h/2$)						
3D(θ_a)	0.6479	1.6264	1.3680	0.8175	0.3458	0.1743
3D(θ_c,1D)	1.3282	2.0430	1.5665	0.8946	0.3680	0.1838
3D(θ_c,3D)	1.3841	2.0187	1.5592	0.8934	0.3679	0.1838
w[10^{-5}m] at ($\alpha = a/2$, $\beta = b/2$, $z = 0$)						
3D(θ_a)	2.9557	5.8248	7.4366	7.7817	7.6037	7.4685
3D(θ_c,1D)	3.1261	6.2203	7.6461	7.7384	7.3669	7.1651
3D(θ_c,3D)	2.9405	6.1003	7.5992	7.7248	7.3647	7.1646
$\sigma_{\alpha\alpha}$[10^4Pa] at ($\alpha = a/2$, $\beta = b/2$, $z = +h/2$)						
3D(θ_a)	-30.353	-39.796	-63.025	-94.912	-121.52	-131.22
3D(θ_c,1D)	-16.005	-31.260	-63.948	-101.82	-131.33	-141.73
3D(θ_c,3D)	-49.975	-38.883	-65.959	-102.30	-131.40	-141.75
$\sigma_{\beta\beta}$[10^4Pa] at ($\alpha = a/2$, $\beta = b/2$, $z = -h/2$)						
3D(θ_a)	-6.2333	5.5609	34.884	56.468	69.026	72.734
3D(θ_c,1D)	-21.024	0.0635	32.842	54.605	66.248	69.464
3D(θ_c,3D)	-23.195	-0.3048	32.583	54.502	66.227	69.458
$\sigma_{\alpha\beta}$[10^4Pa] at ($\alpha = 0$, $\beta = 0$, $z = +h/4$)						
3D(θ_a)	-53.004	-34.402	-12.851	-2.7306	0.1396	0.2914
3D(θ_c,1D)	-52.233	-28.954	-7.4856	0.7013	1.6463	1.0601
3D(θ_c,3D)	-44.666	-27.810	-7.3394	0.7151	1.6469	1.0601
$\sigma_{\alpha z}$[10^4Pa] at ($\alpha = 0$, $\beta = b/2$, $z = +h/4$)						
3D(θ_a)	11.410	2.8595	-1.3183	-2.0168	-1.1898	-0.6587
3D(θ_c,1D)	11.275	1.2740	-2.7727	-2.8863	-1.5517	-0.8396
3D(θ_c,3D)	7.2149	0.9005	-2.8097	-2.8889	-1.5517	-0.8396
$\sigma_{\beta z}$[10^4Pa] at ($\alpha = a/2$, $\beta = 0$, $z = -h/4$)						
3D(θ_a)	13.084	5.4242	0.6419	-0.6211	-0.4972	-0.2884
3D(θ_c,1D)	12.141	3.6918	-0.6355	-1.3225	-0.7766	-0.4262
3D(θ_c,3D)	11.798	3.6010	-0.6378	-1.3213	-0.7765	-0.4262
σ_{zz}[10^4Pa] at ($\alpha = a/2$, $\beta = b/2$, $z = -h/4$)						
3D(θ_a)	-2.1848	-0.6175	0.5564	0.6729	0.3720	0.2022
3D(θ_c,1D)	2.6622	1.1518	1.5228	1.1590	0.5600	0.2944
3D(θ_c,3D)	3.3096	1.1724	1.5195	1.1579	0.5599	0.2944

Table 11: Eighth benchmark, simply-supported three-layered isotropic Al2024/Ti22/Steel spherical shell with external sovra-temperature amplitudes $\Theta_t = 1.0K$ and $\Theta_b = 0.0K$ ($m = n = 1$). Proposed 3D thermo-elastic solution uses order $N = 3$ for the exponential matrix and $M = 300$ mathematical layers.

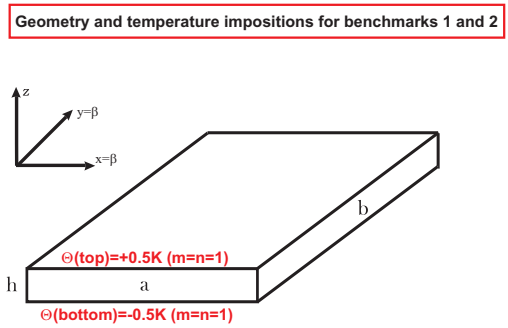

Figure 1: Benchmarks 1 and 2: plate geometry and applied temperature.

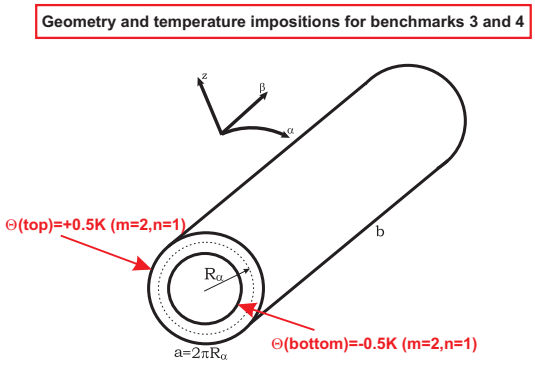

Figure 2: Benchmarks 3 and 4: cylinder geometry and applied temperature.

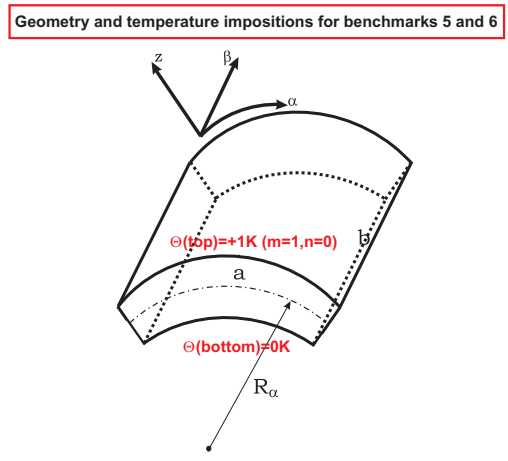

Figure 3: Benchmarks 5 and 6: cylindrical shell geometry and applied temperature.

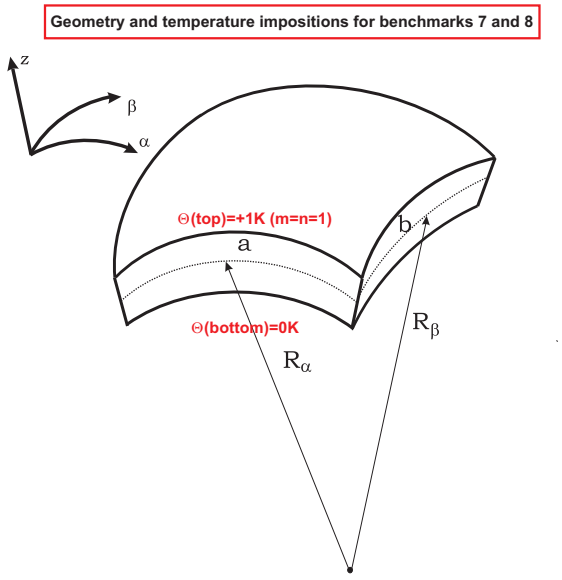

Figure 4: Benchmarks 7 and 8: spherical shell geometry and applied temperature.

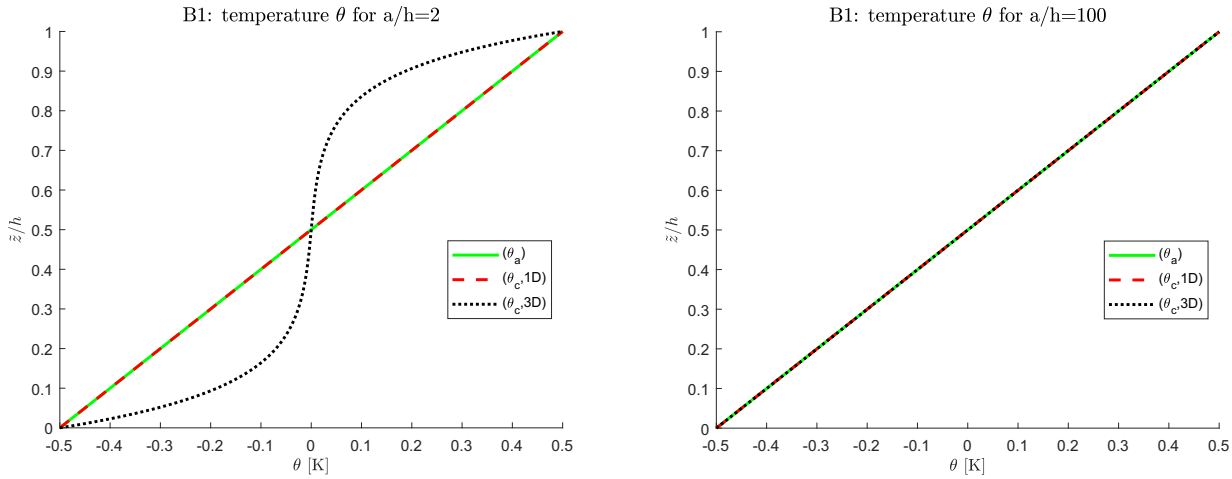

Figure 5: First benchmark, temperature profiles for thick (on the left) and thin (on the right) one-layered 0° composite square plate. The maximum amplitude of the temperature $\theta(\alpha, \beta, z)$ is evaluated at $(a/2,b/2)$.

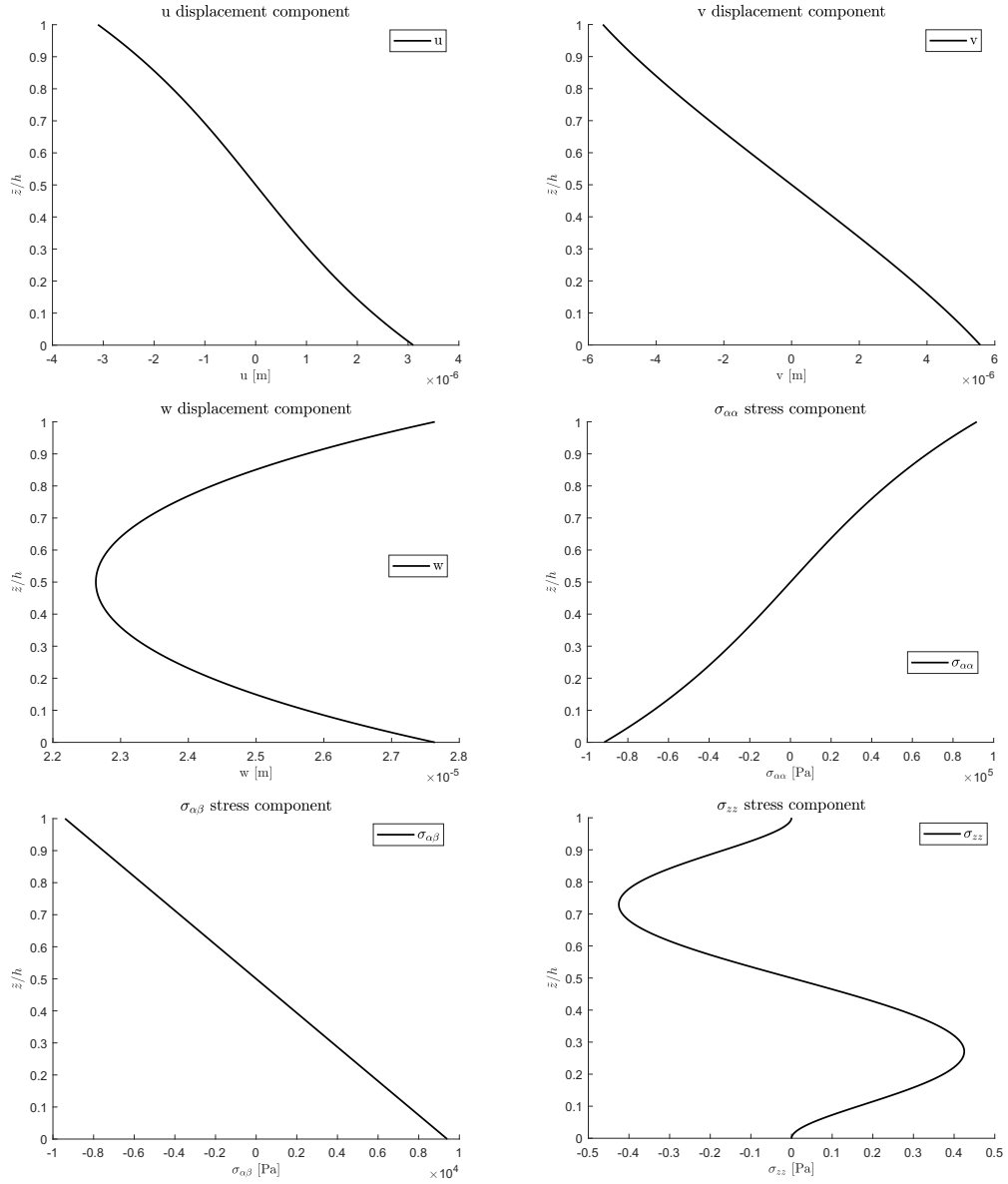

Figure 6: First benchmark, displacements and stresses for thick (a/h=10) one-layered 0° composite square plate obtained via a 3D exact model based on a 3D calculated temperature profile (θ_c,3D). Maximum amplitudes: w, $\sigma_{\alpha\alpha}$ and σ_{zz} at ($a/2$,$b/2$); u at (0,$b/2$); v at ($a/2$,0); $\sigma_{\alpha\beta}$ at (0,0).

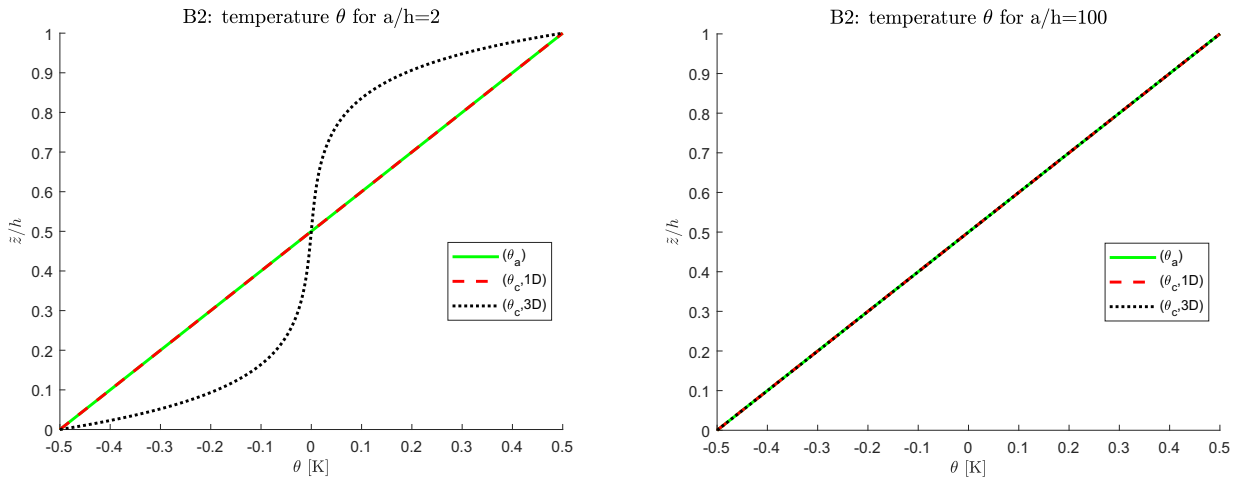

Figure 7: Second benchmark, temperature profiles for thick (on the left) and thin (on the right) three-layered $0°/90°/0°$ composite square plate. The maximum amplitude of the temperature $\theta(\alpha, \beta, z)$ is evaluated at ($a/2$,$b/2$).

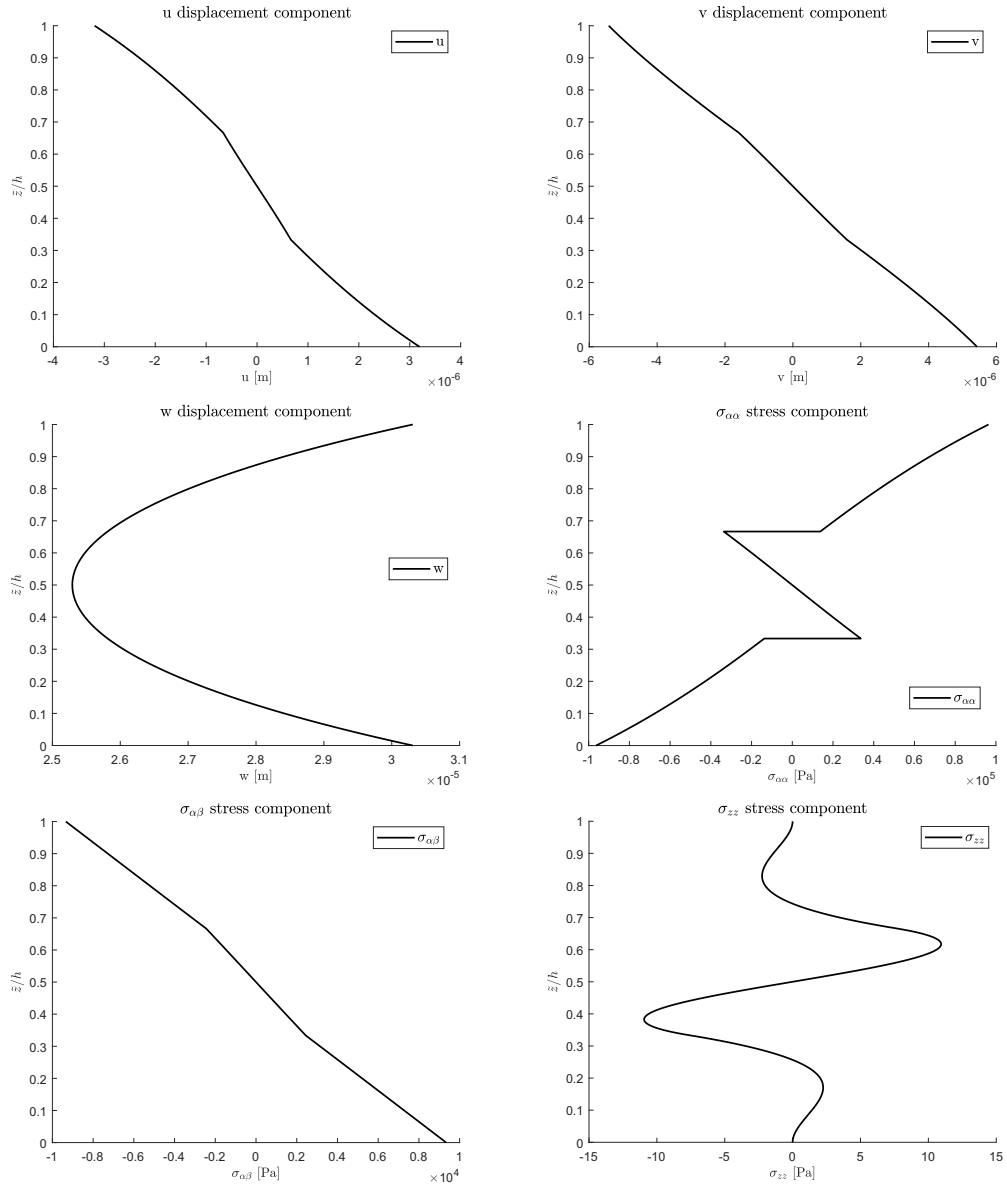

Figure 8: Second benchmark, displacements and stresses for thick (a/h=10) three-layered 0°/90°/0° composite square plate obtained via a 3D exact model based on a 3D calculated temperature profile (θ_c,3D). Maximum amplitudes: w, $\sigma_{\alpha\alpha}$ and σ_{zz} at ($a/2$,$b/2$); u at (0,$b/2$); v at ($a/2$,0); $\sigma_{\alpha\beta}$ at (0,0).

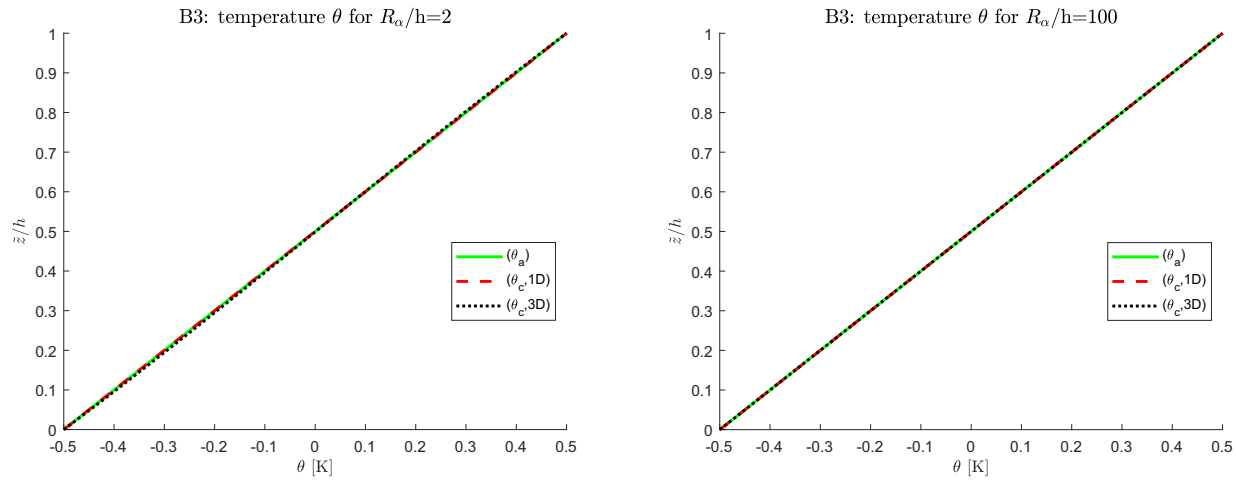

Figure 9: Third benchmark, temperature profiles for thick (on the left) and thin (on the right) one-layered isotropic Al2024 cylinder. The maximum amplitude of the temperature $\theta(\alpha, \beta, z)$ is evaluated at (a/2,b/2).

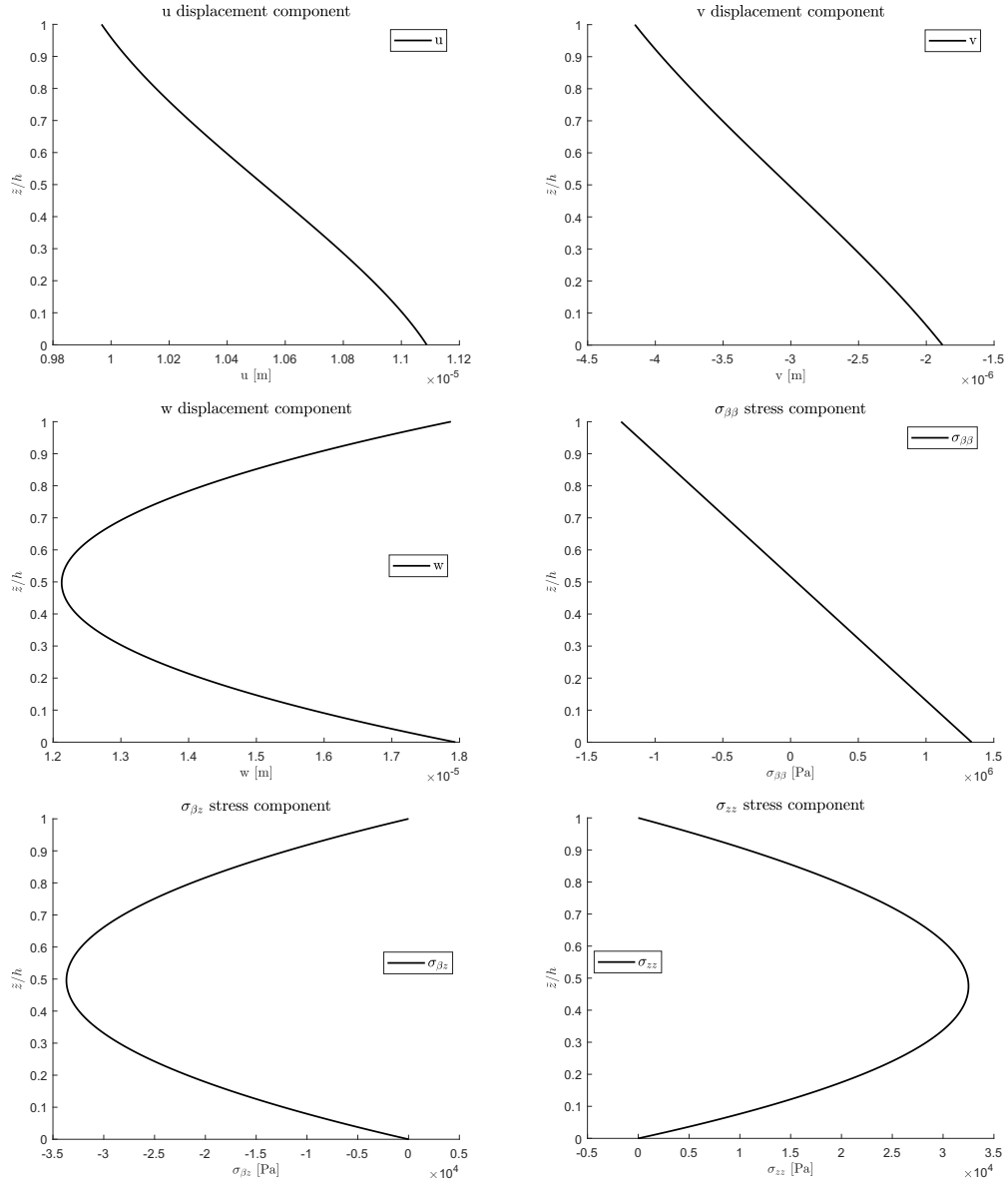

Figure 10: Third benchmark, displacements and stresses for thick (R_α/h=10) one-layered isotropic Al2024 cylinder obtained via a 3D exact model based on a 3D calculated temperature profile (θ_c,3D). Maximum amplitudes: w, $\sigma_{\beta\beta}$ and σ_{zz} at ($a/2$,$b/2$); u at (0,$b/2$); v and $\sigma_{\beta z}$ at ($a/2$,0).

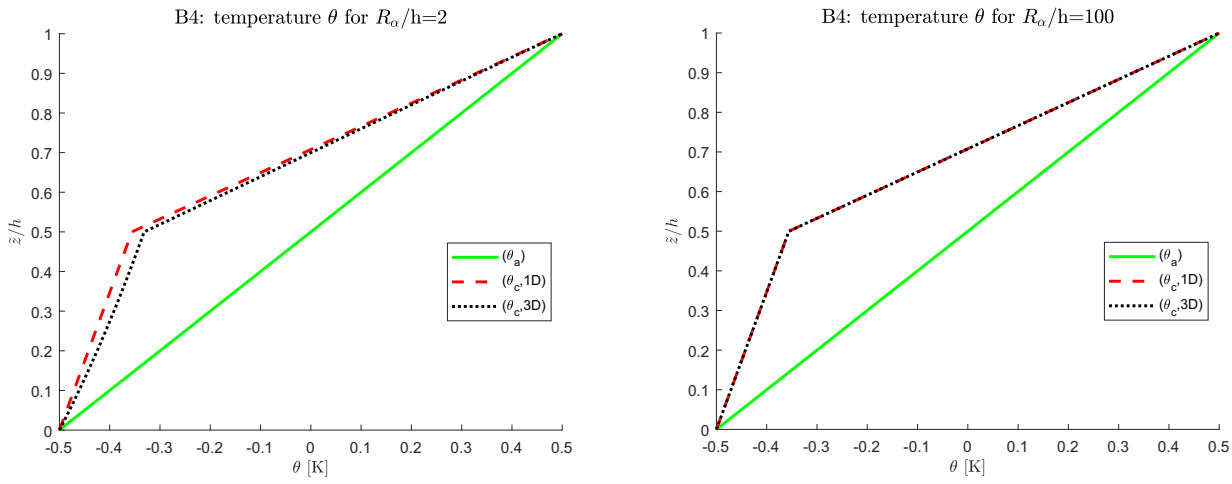

Figure 11: Fourth benchmark, temperature profiles for thick (on the left) and thin (on the right) two-layered isotropic Al2024/Ti22 cylinder. The maximum amplitude of the temperature $\theta(\alpha, \beta, z)$ is evaluated at (a/2,b/2).

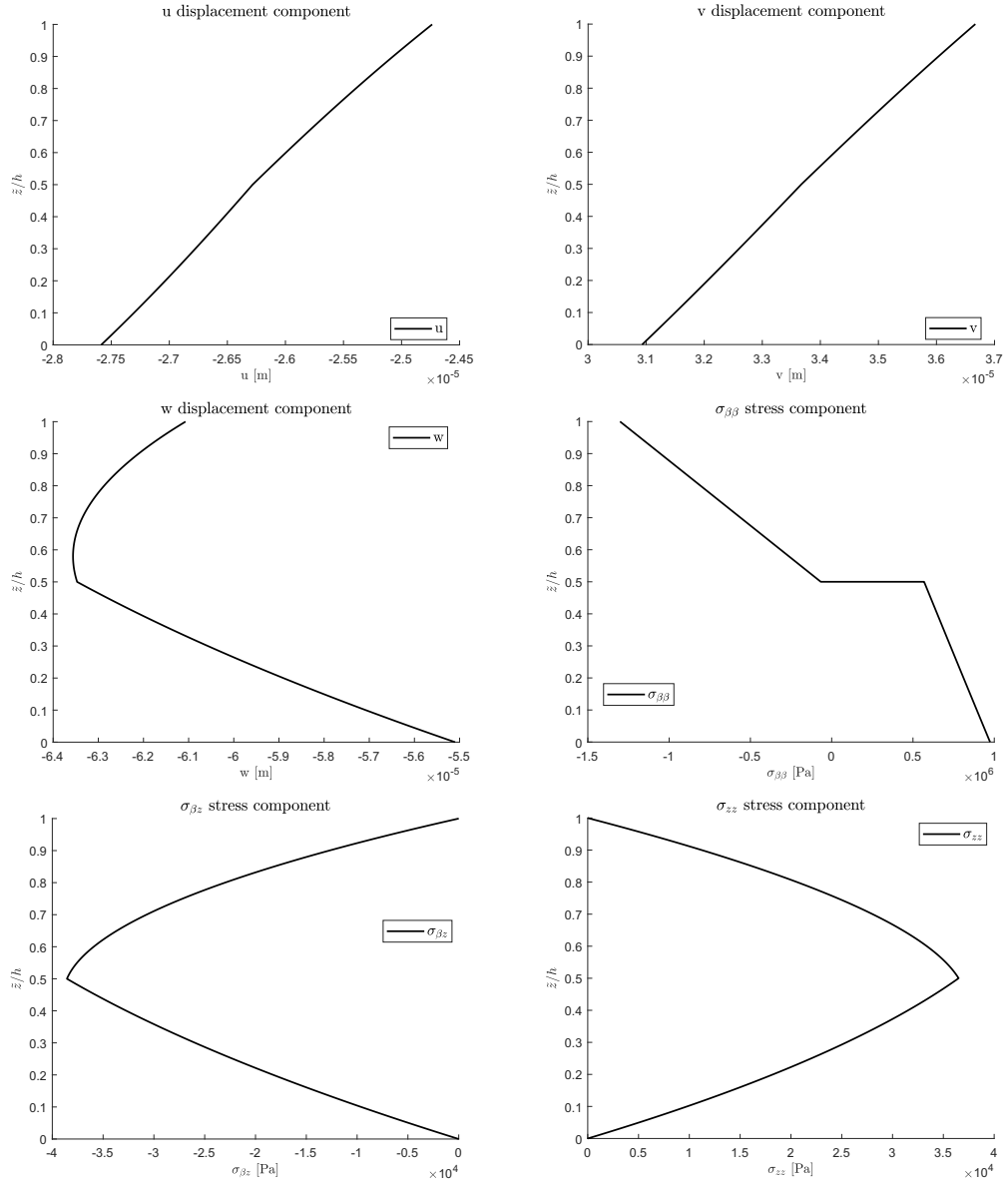

Figure 12: Fourth benchmark, displacements and stresses for thick (R_α/h=10) two-layered isotropic Al2024/Ti22 cylinder obtained via a 3D exact model based on a 3D calculated temperature profile (θ_c,3D). Maximum amplitudes: w, $\sigma_{\beta\beta}$ and σ_{zz} at (a/2,b/2); u at (0,b/2); v and $\sigma_{\beta z}$ at (a/2,0).

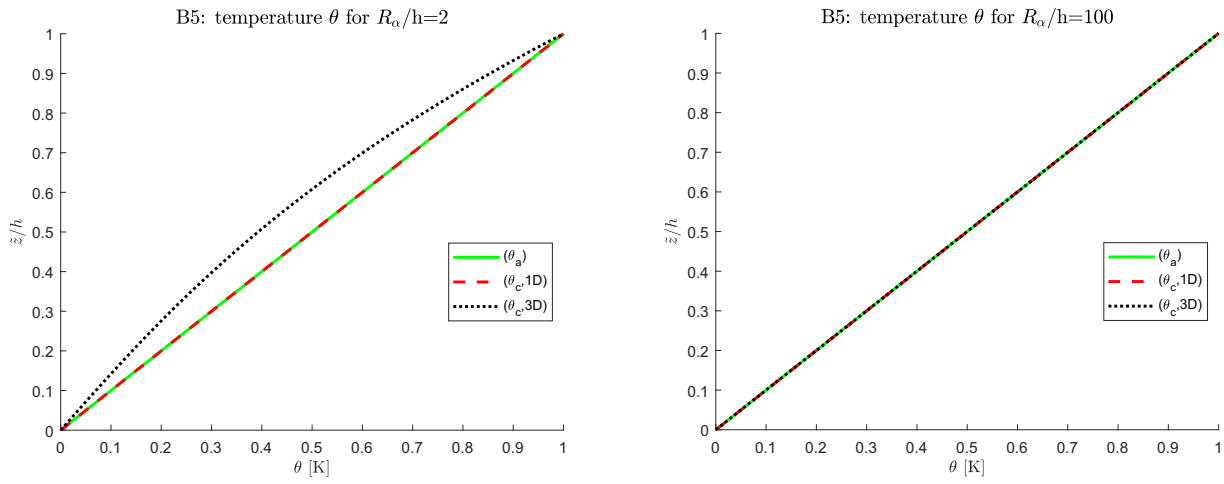

Figure 13: Fifth benchmark, temperature profiles for thick (on the left) and thin (on the right) one-layered isotropic Ti22 cylindrical shell. The maximum amplitude of the temperature $\theta(\alpha, \beta, z)$ is evaluated at ($a/2$,$b/2$).

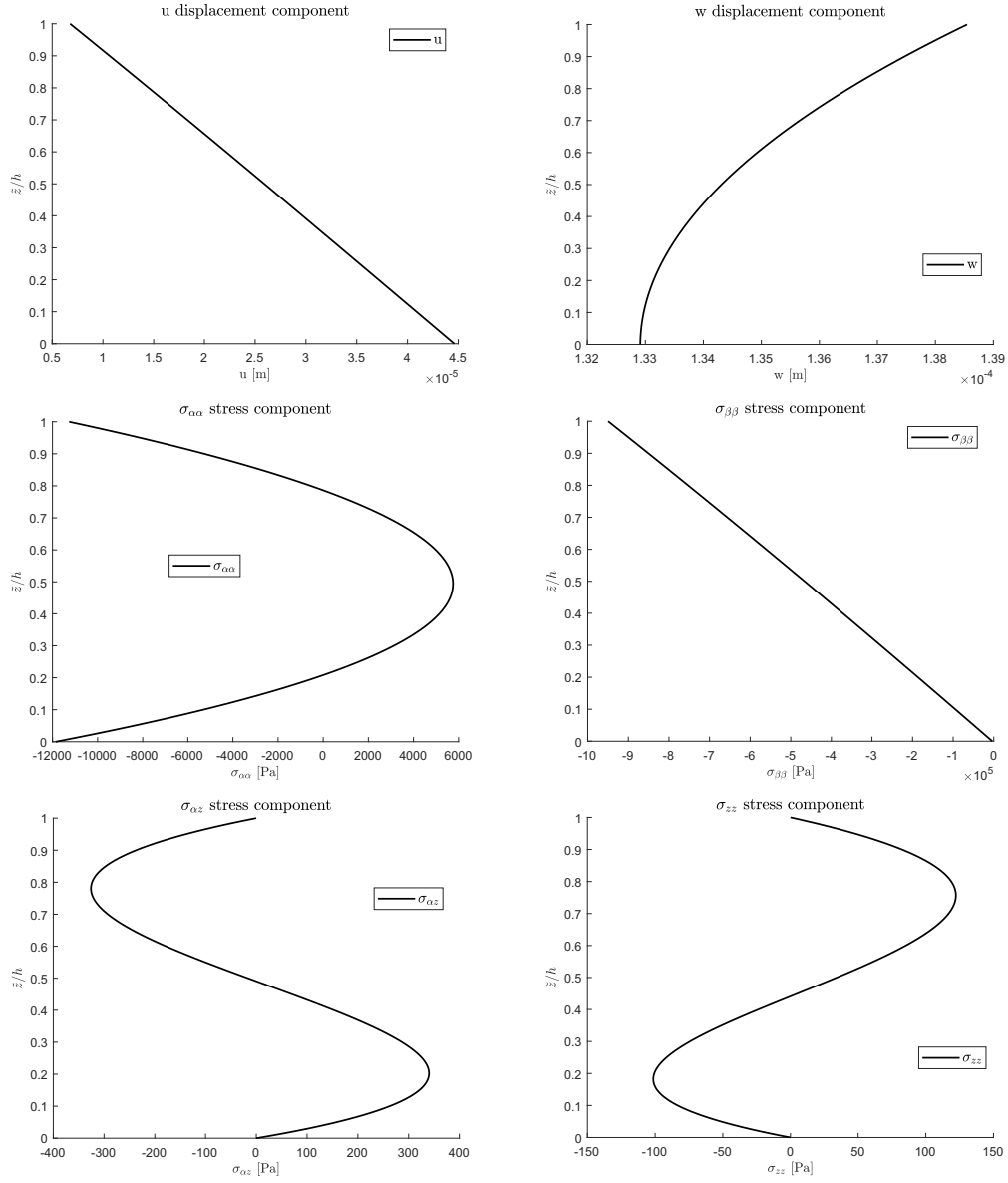

Figure 14: Fifth benchmark, displacements and stresses for thick (R_α/h=10) one-layered isotropic Ti22 cylinder obtained via a 3D exact model based on a 3D calculated temperature profile (θ_c,3D). Maximum amplitudes: w, $\sigma_{\alpha\alpha}$, $\sigma_{\beta\beta}$ and σ_{zz} at ($a/2$,$b/2$); u and $\sigma_{\alpha z}$ at (0,$b/2$).

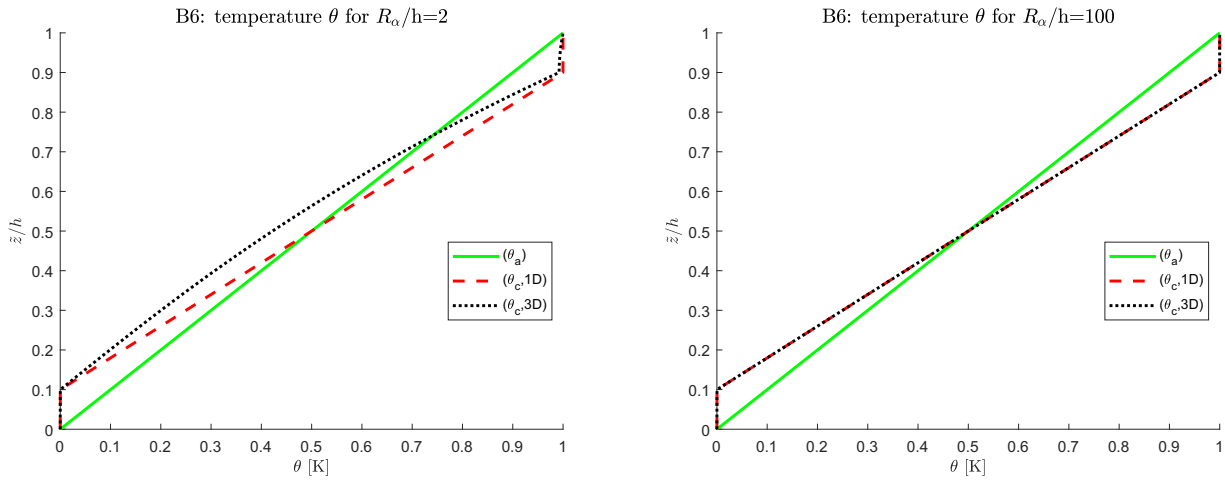

Figure 15: Sixth benchmark, temperature profiles for thick (on the left) and thin (on the right) sandwich Al2024/PVC/Al2024 cylindrical shell. The maximum amplitude of the temperature $\theta(\alpha, \beta, z)$ is evaluated at ($a/2$,$b/2$).

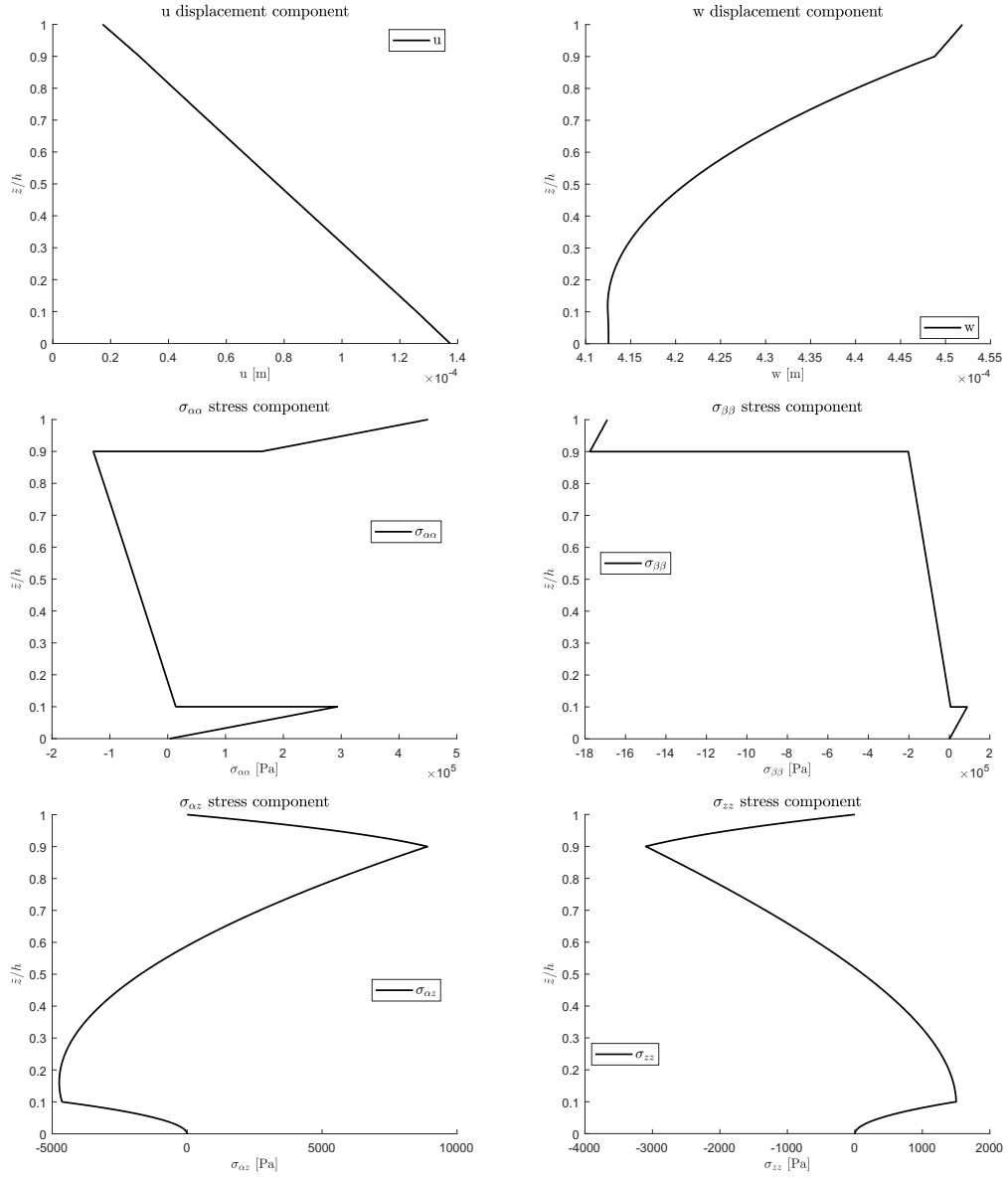

Figure 16: Sixth benchmark, displacements and stresses for thick (R_α/h=10) sandwich Al2024/PVC/Al2024 cylinder obtained via a 3D exact model based on a 3D calculated temperature profile (θ_c,3D). Maximum amplitudes: w, $\sigma_{\alpha\alpha}$, $\sigma_{\beta\beta}$ and σ_{zz} at ($a/2$,$b/2$); u and $\sigma_{\alpha z}$ at (0,$b/2$).

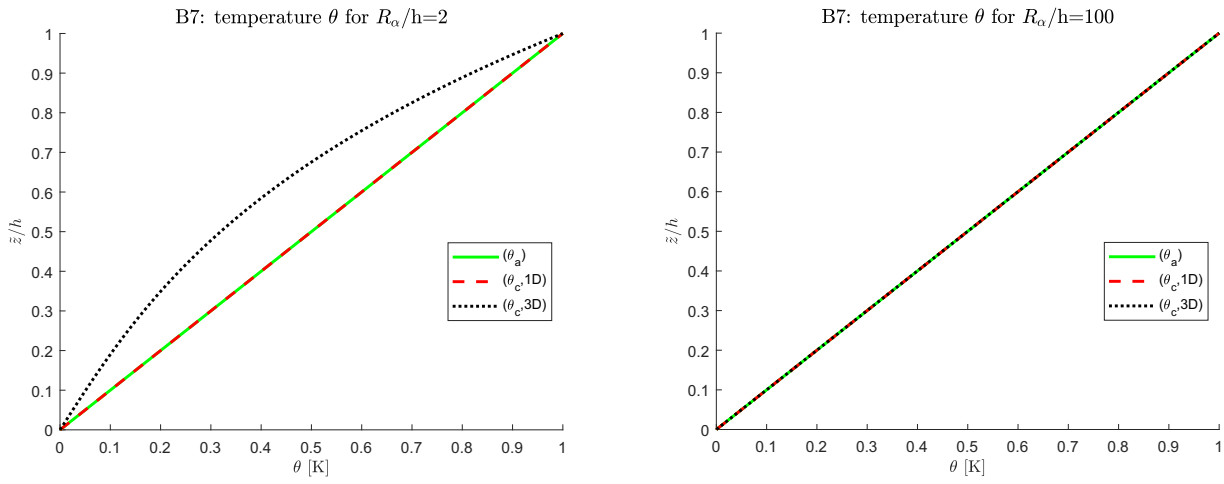

Figure 17: Seventh benchmark, temperature profiles for thick (on the left) and thin (on the right) one-layered isotropic Steel spherical shell. The maximum amplitude of the temperature $\theta(\alpha, \beta, z)$ is evaluated at $(a/2,b/2)$.

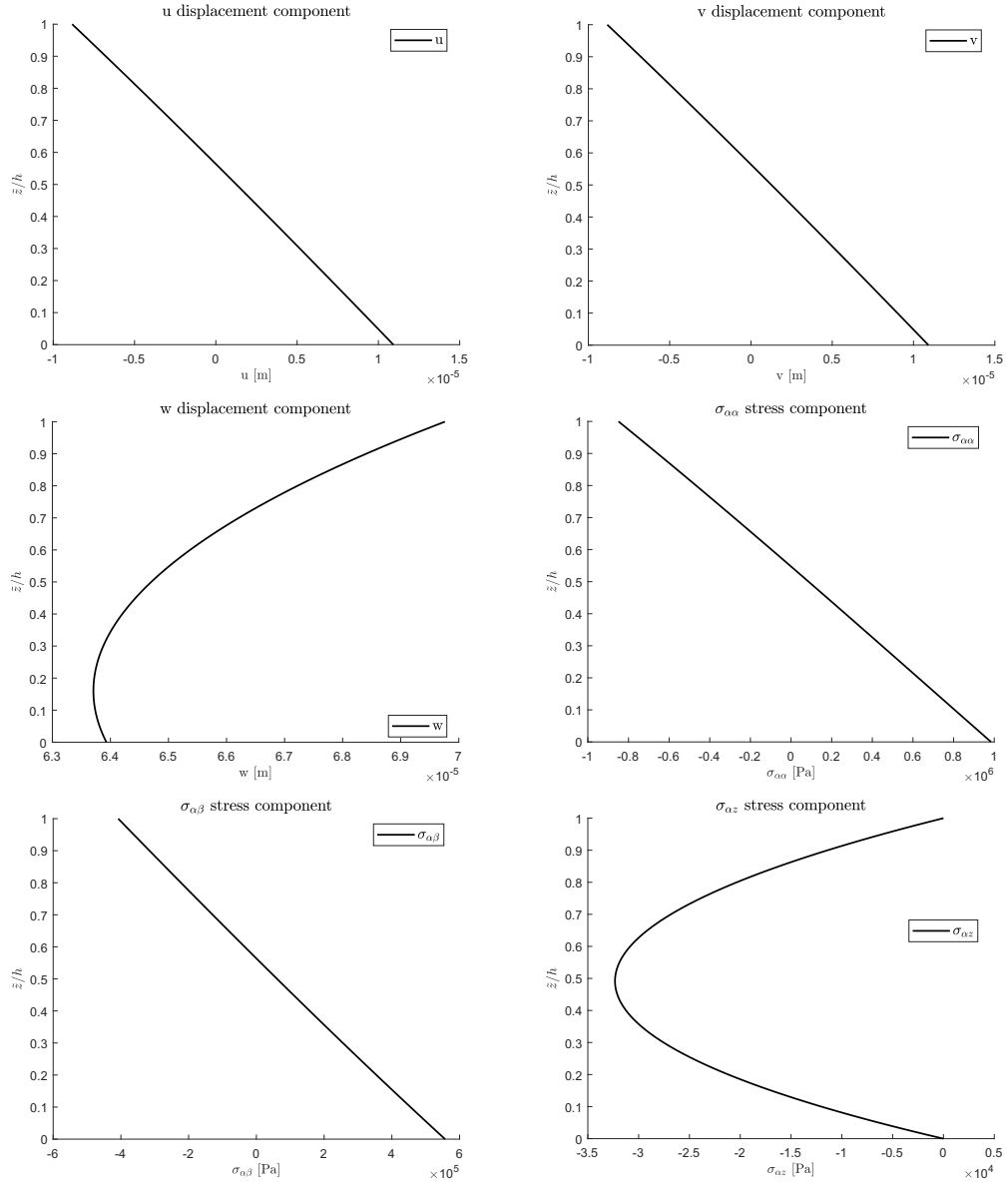

Figure 18: Seventh benchmark, displacements and stresses for thick (R_α/h=10) one-layered isotropic Steel spherical shell obtained via a 3D exact model based on a 3D calculated temperature profile (θ_c,3D). Maximum amplitudes: w and $\sigma_{\alpha\alpha}$ at (a/2,b/2); u and $\sigma_{\alpha z}$ at (0,b/2); v at (a/2,0); $\sigma_{\alpha\beta}$ at (0,0).

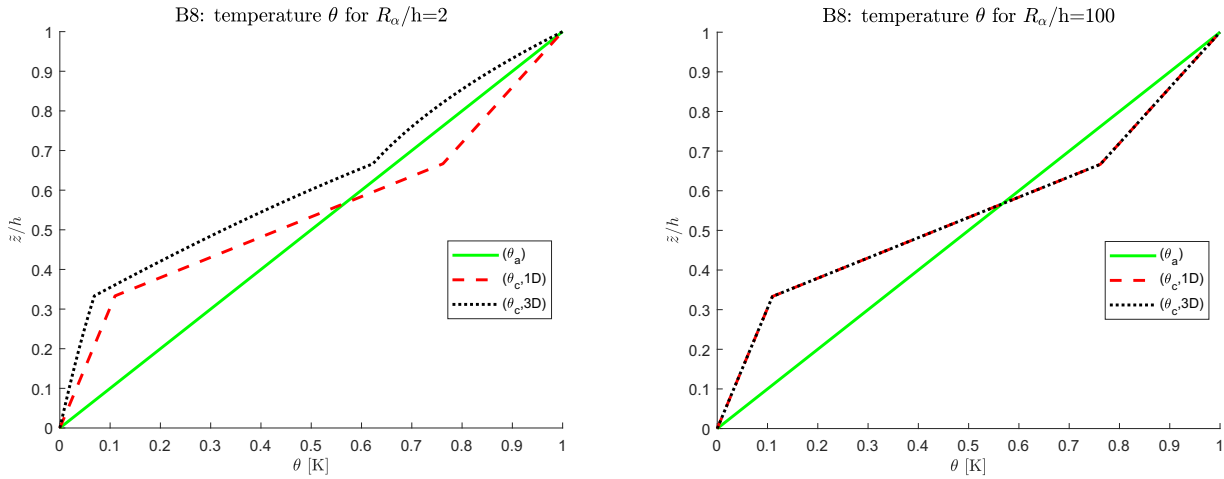

Figure 19: Eighth benchmark, temperature profiles for thick (on the left) and thin (on the right) three-layered isotropic Al2024/Ti22/Steel spherical shell. The maximum amplitude of the temperature $\theta(\alpha, \beta, z)$ is evaluated at (a/2,b/2).

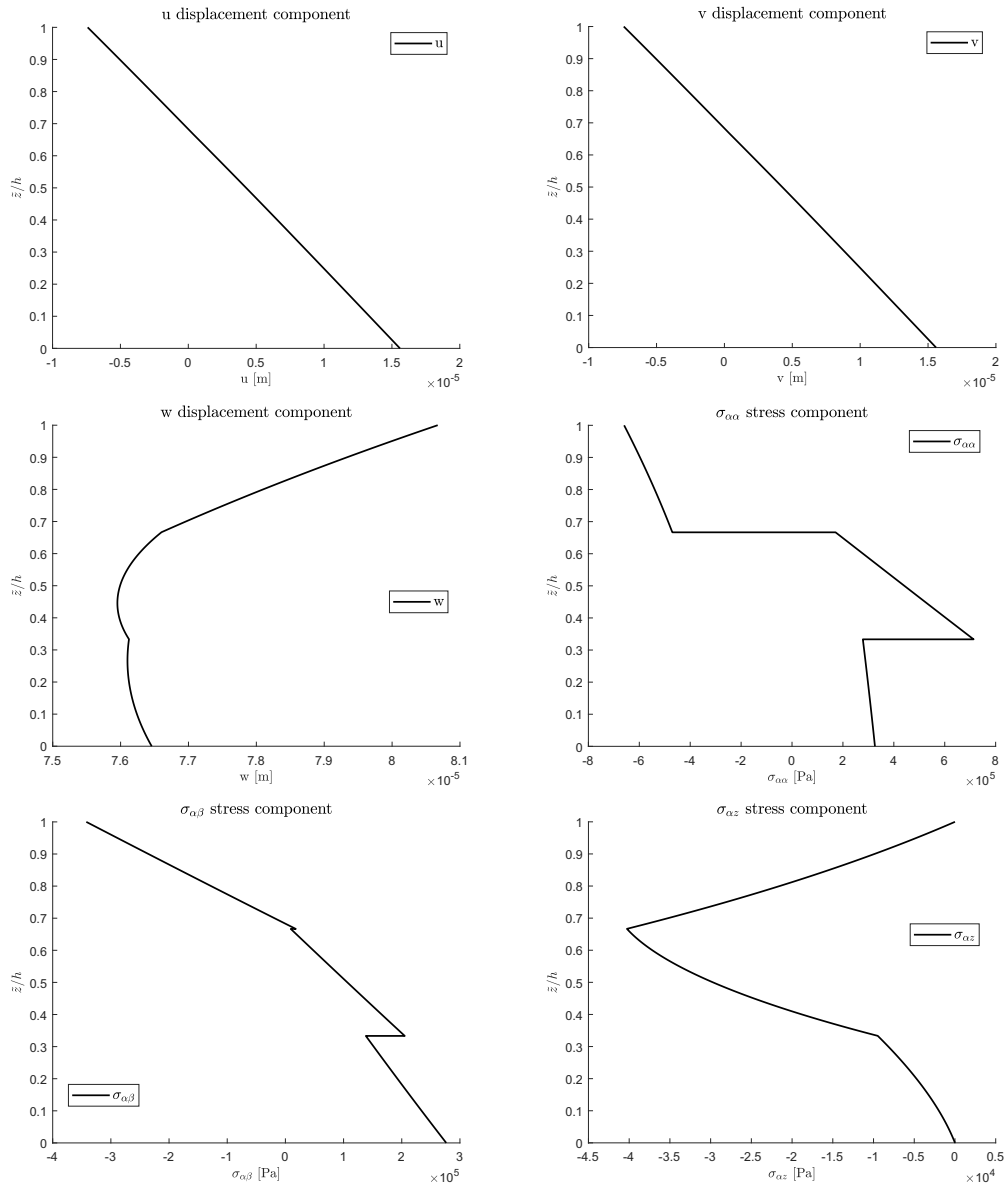

Figure 20: Eighth benchmark, displacements and stresses for thick (R_α/h=10) three-layered isotropic Al2024/Ti22/Steel spherical shell obtained via a 3D exact model based on a 3D calculated temperature profile (θ_c,3D). Maximum amplitudes: w and $\sigma_{\alpha\alpha}$ at ($a/2$,$b/2$); u and $\sigma_{\alpha z}$ at (0,$b/2$); v at ($a/2$,0); $\sigma_{\alpha\beta}$ at (0,0).